# BRNO UNIVERSITY OF TECHNOLOGY

## FACULTY OF MECHANICAL ENGINEERING

## INSTITUTE OF SOLID MECHANICS, MECHATRONICS AND BIOMECHANICS

## ANALYSIS OF INFLUENCE OF BLOOD FLOW AND ARTERIAL GEOMETRY ON PATHOLOGICAL PROCESSES IN ARTERIES

ANALÝZA VLIVU PROUDĚNÍ KRVE A GEOMETRICKÉHO USPOŘÁDÁNÍ NA PATOLOGICKÉ PROCESY V TEPNÁCH

### DOCTORAL THESIS SUMMARY
TEZE DIZERTAČNÍ PRÁCE

| | |
|---|---|
| **AUTHOR**<br>AUTOR PRÁCE | Ing. Jiří Jagoš |
| **SUPERVISOR**<br>ŠKOLITEL | prof. Ing. Jiří Burša, Ph.D. |

BRNO 2023

# Contents

# 1. Introduction - motivation of the research

*... at the beginning a disease is easy to cure but difficult to diagnose; but as time passes, not having been treated or recognized at the outset, it becomes easy to diagnose but difficult to cure ... (*Niccolo Machiavelli, *Il Principe*, 1513)

Although the citation is several hundred years old, unfortunately, it is still true. Even in such fast-growing field as a medicine. Notwithstanding that humanity has almost eradicated some deadly diseases, others have arrived. Our body has a tremendous complexity together with a great subject-to-subject variability. Probably for these reasons, we have not been able to understand and consequently prevent all of the diseases yet. And in my opinion, it will be never possible. However, we can try to minimize their incidence, mortality or severity of their consequences and to prolong thus a life expectancy but, mainly, to ensure a dignified and active aging.

*A man is as old as his arteries. (*Thomas Sydenham)

The second quotation is also very actual today. Life expectancy has more than doubled in the last one hundred and fifty years and the most common causes of death are so-called diseases of old age, *i.e.*, cardiovascular diseases [1][2]. Although the occurrence of these diseases is largely conditioned by genetics (*i.e.*, family history) and age, development of diseases of civilization (atherosclerosis, hypertension, overweight, diabetes mellitus, cancer, etc.) occurs often within individuals under 40 years of age. This assures us that we can largely contribute to the possible emergence or suppression of the development of the disease by ourselves. Most of these diseases of civilization, if not being directly cardiovascular diseases, represent their significant risk factors. A common feature of both types of these diseases is they have a significant effect on the degradation of arterial structure (either as a consequence or as a cause) and are often referred to as accelerated aging. On the other hand, regular exercise, healthy food without excessive salt and alcohol consumption and smoking cessation act as an effective prevention against these diseases.

One of the main goals of this work is to strengthen the set of risk factors for cardiovascular diseases, on the basis of which it is possible to identify a high-risk patient, send him to in-depth examination where a particular disease is confirmed or refuted. Early identification of the disease will significantly increase the chances of its suppression. This work focuses on an occlusive disease of the arteries (*i.e.*, atherosclerosis) and, conversely, a disease causing artery dilation, an aneurysm. In case of the worst scenarios, the former ends with a myocardial infarction or stroke while the latter may result in a massive internal bleeding which is usually fatal or at least, the subject becomes functionally dependent. For instance, the aneurysm in the infrarenal aorta, if ruptured, has the highest mortality of all, reaching up to 90% [3]. Moreover, both diseases are mostly asymptomatic for a very long time and occur mainly in the population above 55 years [4,5]. Of course it is not possible to scan regularly all this population in order to monitor if the aneurysms and/or atherosclerosis are developing or not. Therefore, a large effort has been done to identify patients at enhanced risk of developing these diseases. During last decades, the most relevant risk factors were identified: male sex, age, smoking status, hypertension and family history. These factors can be easily identified without any additional examination and patients with high-risk score can be further examined (preferentially using ultrasound). Nevertheless, in case of the atherosclerosis, most heart attacks and strokes occur at people at averaged risk-factor level who are classified as low or intermediate risk according

to traditional risk factor scoring [6]. Similar findings can be found in retrospective study [7] of small aneurysms (*i.e.*, ranked as low-risk) with subarachnoid hemorrhage (SAH). For this reason, there is still a need of further refinement of the risk factors to decrease a rate of these misclassification.

**This thesis aims: (i) to create a credible computational model of pulsatile blood flow in arteries, including its validation with experiments; (ii) to create an experimental circuit simulating pulse wave propagation (PWV) in a compliant tube and in (iii) consequent exploitation of the created model for fluid-structure interaction (FSI) analyses of human aortic tree and finally, (iv) to create a 3D computational fluid dynamics (CFD) patient-specific (PS) model of human carotid arteries with lumped parameters boundary conditions (BCs).**

# 2. Research background

## 2.1. Cardiovascular system hemodynamics

Cardiovascular system consists of the heart, blood and network of blood vessels, namely arteries, arterioles, capillaries, capillary beds, venules and veins. Its crucial function is to maintain homeostasis and favourable cellular environment via circulation of blood. The second crucial function of the circulatory system is to move an oxygenated blood away from heart via arteries provide required amount of nutrients and oxygen for all vital organs. Simultaneously, carbon dioxide, waste product and de-oxygenated blood are removed and transported through the venules and veins towards the heart and other organs where they are cleaned up [8,9]. This exchange is done within the microcirculation, the most peripherical part of the system. And finally, the arterial tree, as a part of the cardiovascular system has to transform the highly pulsatile nature of flow generated by ventricular ejection in large vessels (with relatively high mean velocities ~ 20 cm/s) into quasi stationary flow (with mean velocities ~ 0.03 cm/s) at the arteriolar and capillary level (see Figure 1A). This transformation of the flow waveform provides suitable conditions for proper diffusion since the exchange of the oxygen, nutrients and waste products between blood and the surrounding tissue is rather diffusive [8,10]. On the contrary, the pressure wave amplitude (and systolic pressure) and steepness of the front part of the waveform increase as we move towards the periphery within the arterial tree [11,12]. Only a slow decrease in the mean pressure is observed (see Figure 1B) [8,10,12].
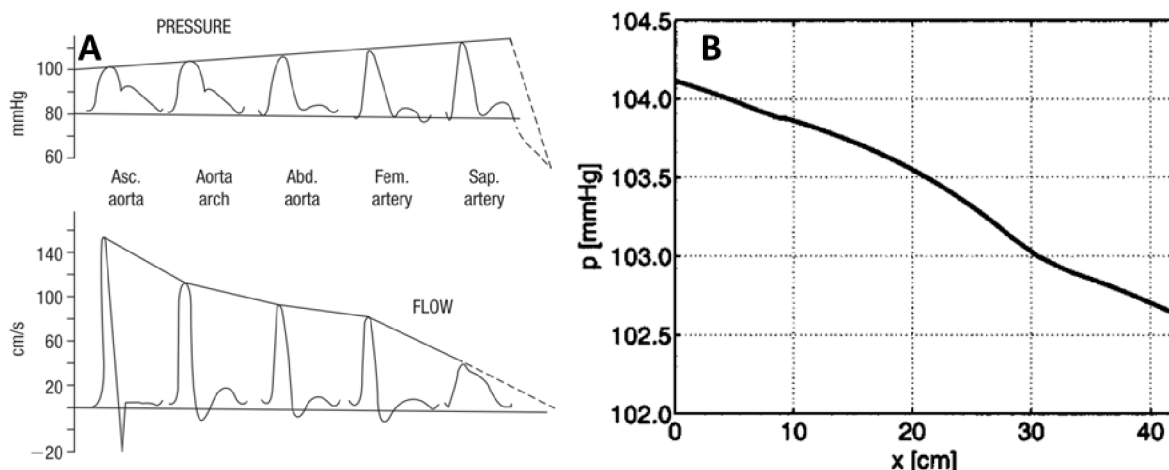


*Figure 1 A) – Schematic of pressure and velocity waves as they travel towards the periphery. While the velocity waves are damped out in relative consistent manner, an amplitude of the pressure waves increases up to the saphenous artery and then decreases sharply (see broken line). Adopted from [11]. B) – Although the amplitude of the pressure waves increases, mean pressure falls slowly (x axis represents a distance from the heart). Adopted from [12].*

The large arteries are highly compliant (e. g. proximal aorta alone represents ~ 60% of the total arterial compliance [13]) and geometrically complex vessels. The significant compliance causes marked two-way interaction between vessel wall and blood flow. Furthermore, the pressure and velocity wave travel with some finite velocity **c**, *i.e.*, pulse wave velocity (PWV). PWV observed clinically for a normotensive middle-aged subject increases from 5 m.s$^{-1}$ in the thoracic aorta to 6 m.s$^{-1}$ in the abdominal aorta (AA) and to 9 m.s$^{-1}$ in the iliac and femoral arteries [14].

## 2.2. Arterial wall structure

Arteries can be divided into elastic, muscular and intermediate. Main constituents of the artery wall are elastin and collagen (50% of dry weight); the rest consists of smooth muscle cells and non-fibrous matrix [11]. The elastic arteries are located close to heart with elastin as a dominant component of the wall while the muscular arteries are located at the periphery where collagen fibres dominate [11]. Since the elastic modulus of collagen is more than 300 times higher than elastin modulus (~ 100 MPa vs 0.3 MPa), stiffness of arteries increases towards the periphery [11]. The normal arterial wall consists of three concentric layers: tunica intima, t. media and t. adventitia (see Figure 2A, B).
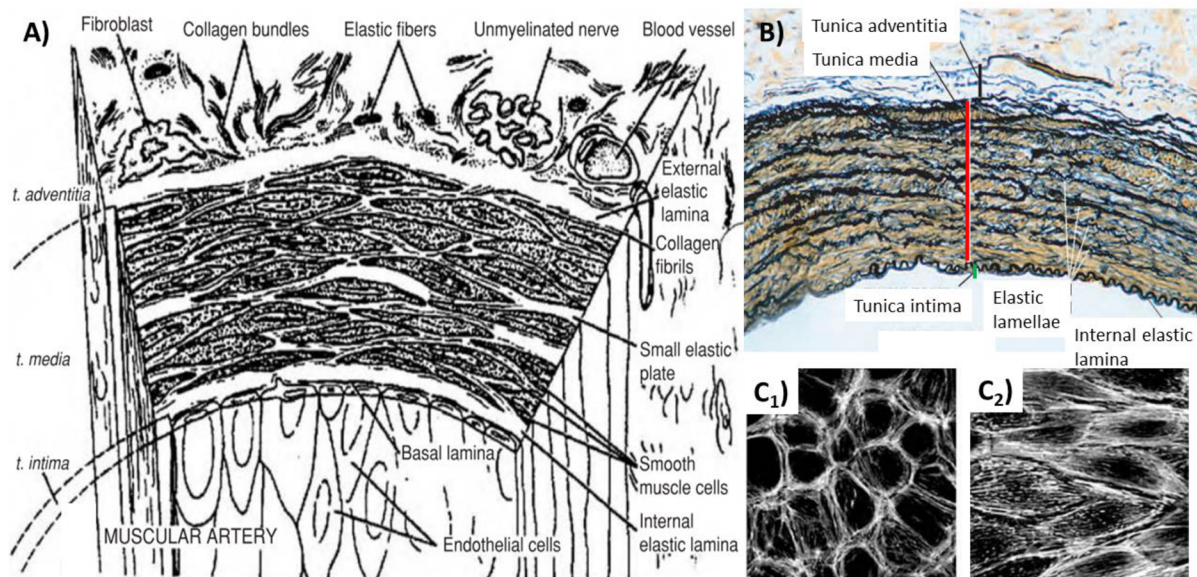


*Figure 2 Structure of the multi-layered artery wall. Schematic (A) versus real (B) histological section through an artery wall. Figures (C$_{1-2}$) showing remodelling of the endothelial cells after being exposed to shear stress of 1.5 Pa for 48 h. Modified from* [10]*.*

The innermost (blood-contacting) layer, the intima, is only a few micrometres thick (in a healthy artery) and consists of a monolayer of endothelial cells attached to basal lamina. The basal lamina is composed from collagen, fibronectin and laminin [10,15]. The endothelium monolayer acts as a selectively permeable barrier which regulates the transport of macromolecules between vascular lumen (*i.e.*, blood) and vascular smooth muscle through the muscle cells themselves (in a diffusive manner) or through cell-to-cell junctions [16]. They are subjected to pulsatile wall shear stress from the blood flow and also to a cyclic strain from the pulsatile pressure induced by the heart. The endothelial cells sense these mechanical stimuli and play a significant role in the local regulation of vascular tone via smooth muscle cells to preserve homeostasis [10]. Under physiological conditions, endothelial cells are long flat cells oriented along the vessel axis (see Figure 2C2). This configuration can be characterized as a tight junction [16]. If the process of homeostasis is disrupted and the endothelium is no longer

capable to preserve the optimal wall shear stresses and strains, the endothelium cells become rounder with a non-uniform orientation and greater permeability (see Figure 2C1) resulting in conditions which are linked with genesis of some cardiovascular diseases [16–19]. The middle layer (media) is separated from the intima by a thin elastin-rich ring known as the internal elastic lamina (see Figure 2A, B) [10]. Media consists of smooth muscle cells embedded in an extracellular matrix composed of elastin, multiple types of collagen, and proteoglycans [10,15]; finally, the outermost layer (adventitia) consists of a loose connective tissue that contains collagen, nerves, fibroblasts, and some elastin fibers [10,15]. Boundary between the media and adventitia is defined by external elastic lamina (see Figure 2A). The adventitia keeps the arteries attached to the surrounding connective tissue [10].

## 2.3. The most common cardiovascular causes of death

Cardiovascular diseases (*i.e.*, diseases of the heart and circulatory system) are the most frequent causes of death in the US [20,21] and also in the EU [22] with coronary heart disease ranked as the most frequent one. Stroke (both ischemic and hemorrhagic, *i.e.*, representing two different diseases related to degeneration of blood vessels) was ranked as the fifth most frequent cause of death in the US in 2017 [20] and even second single most common cause of death in the EU [22]. Atherosclerosis plaque rupture can cause total occlusion of the vessel and consequently, heart attack or stroke [11], depending on the location of the plaque within the arterial tree. Since atherosclerosis preferentially develops at arterial branches and curvatures [19], it can be frequently found at the outer wall along carotid sinus or at the aortic bifurcation. As regard to the latter, here the plaque rupture does not lead to heart attack or stroke whereas resulting in a critical limb ischemia (CLI). Furthermore, CLI is associated with major health complications and may lead up to lower limb amputation. The same area of arterial tree is also often affected by aortic aneurysms. They are frequently found also within intracranial arteries, where they are called cerebral. The cerebral aneurysm (CA) rupture is leading mostly to nontraumatic SAH, an event with high rate of severe morbidity and mortality (*i.e.*, 30 – 50%) [23–25]. Although preventable, hypertension and hypertensive renal disease remain another major cause of death globally and also in the developed world, with direct risk for cardiovascular diseases (CVDs) [2,11,26,27]. Finally, it is generally accepted that all the mentioned diseases are closely related, and one can accelerate or initiate development of the another. Thus, focus only on the disease being the most frequent cause of death and underestimation of the others could be misleading.

## 2.4. Numerical modelling of blood flow in arteries

Cardiovascular modelling based on mathematical representation has a long history. Lumped models (also referred as 0D or Windkessel among the literature) are the simplest and the oldest ones and typically represent electrical networks. The utilization of these models in cardiovascular modelling was started by Otto Frank in 1899 [28], who set up an analogy between electrical networks and cardiovascular system. The first model was the two-element Windkessel (2WK) consisting of a compliance C of a part of arterial tree represented by a capacitor whereas their resistance R is described by a resistor. Upgraded version of this model incorporated another element which represents characteristic impedance Z (also referred as $R_p$) to form three-element Windkessel (3WK). The characteristic impedance Z (or $R_p$) in the 3WK, can be seen as a link between the lumped Windkessel model and wave travel aspects of the arterial system. Noordergraaf and co-workers [29] designed and constructed a model of the human systemic tree with distributed properties based on Windkessel principle. Several distributed models based on this prototype had been designed but I will only mention that one

developed by Westerhof et al. [30], because their proposed changes greatly improved the model performance compared to [29] and complied very well with its real counterpart.

Regardless of the success and simplicity of a 0D approach, another approach started to develop nearly in parallel. Its foundation was set by Taylor during 1950s, who designed and constructed simple tubular model with fluid oscillation in an elastic pipe based on Womersley solution [11]. Main advantage was that this approach was continuous (*i.e.*, 1D) where the wave propagation and reflection were considered whereas 0D was a discrete approach. This methodology has been developed into a sophisticated 1D structural model of the whole arterial tree using non-invasive measurements of flow waveform which serves as input BCs together with considering patient-specific (PS) dimensions of most of the larger vessels in humans (e.g., [12]).
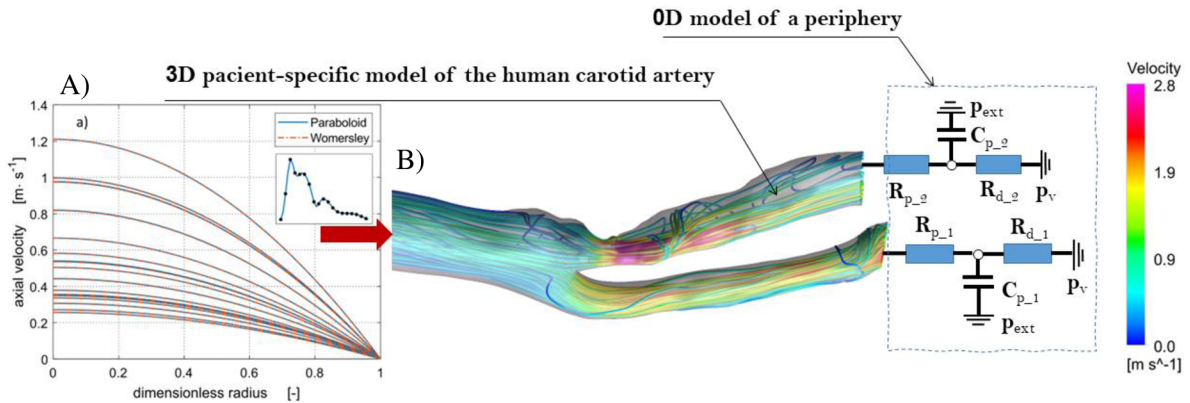


*Figure 3 Example of multiscale model. A) 3D paraboloidal velocity profile used as an input boundary condition. B) A three-element Windkessel model coupled to the 3D model.*

Neither 0D nor 1D models solve detailed flow patterns. To overcome this, a 1D model of larger arteries, for example carotid artery can be replaced with a 3D PS geometry and coupled with 1D or 0D models for its peripheral sites (see Figure 3). A 1D or 0D model of peripheral and venous part of the circulatory system is necessary here due to its excessive complexity for 3D modelling. Such form of simplification is needed not only due to high computational cost (despite of a great progress in this field) which would be the case of 3D PS models of arterial tree considering most larger arteries, but also due to the time necessary for their reconstruction and convergence issues.

On the basis of a review performed on multiscale modelling approaches in the blood flow modelling in large vessels, I can point out that the 3WK model for a periphery (specifically RCR configuration) has become a standard among the most fidelity models [31–33]. It has to be emphasized that estimating of parameters for 3WK is crucial for reaching appropriate PS BCs which represent the remaining circulation. Specifically, we are facing a problem with three unknown parameters per each outlet for the 3WK RCR ($R_p$ – characteristic impedance or proximal resistance; C – compliance and $R_d$ – resistance of a periphery). A general methodology was proposed by Spilker and Taylor [32] and their variations were successfully utilized by many others (e.g., the most recent works [31,34] or the older one reviewed in [33]). The methodology with slight adjustments will be used and described in detail in section 5.2.2.

# 3. Computational model of a pulsatile flow and its validation

Main goals of these experiments were: (i) validation of the computational fluid dynamics (CFD) and fluid-structure interaction (FSI) approaches in the aorta-like tube; (ii) evaluation of the influence of turbulent flow; (iii) assessment of the effect of the wall compliance on the haemodynamic parameters. For a detailed description of such complex flow (pulsatile, transitional), the particle image velocimetry (PIV) measurements across the tube diameter were performed using high-speed camera which enabled us to capture eventual turbulent structures. The following people participated in the work with me: Ing. Michal Kotek, PhD; Ing. Darina Jašíková, PhD; Ing. Jiří Kohút; Prof. Jiří Burša, PhD.

The results of this computational and experimental study have been published in [35] where an information regarding the experimental circuit and numerical simulation can be found in detail.

## 3.1. Main findings

### 3.1.1. Validation of the CFD/FSI approach in the aorta-like tube

The overall agreement of the velocity profiles between the experiment and simulation using the turbulent model is very good for both cases. Discrepancies in the near wall region could be caused due to the relatively coarse radial resolution of the camera. Since the dynamic range and spatial resolution of PIV method is limited by the size of the camera's chip (see [35] for detail), higher small-scale resolution is always accompanied by loosing large-scale picture.

### 3.1.2. Evaluation of the influence of turbulent flow

This work confirms the hypothesis stated in [36] that a longer deceleration phase triggers transition to turbulence while a shorter and more rapid deceleration delayed the transition. In addition, the results are also in accordance with [37] stating that, in a straight rigid tube, turbulent formation takes place in the near wall region and then it diffuses to the core region. In case of the rigid tube, this phenomenon cannot be observed in velocity profiles (see [35]) and neither in peak velocities (see Figure 4A – orange curve representing k-ω SST turbulence model is almost coincident with laminar flow model – blue curve). However, the turbulence is much more significant in the compliant tube, where substantial differences can be observed in both (see [35] for velocity profiles and Figure 4B for peak velocities – blue versus orange curves). Therefore, we put foundations for extension of this hypothesis to compliant tubes while these phenomena were found also here for physiological Reynolds and Womersley numbers. Thus, the length of the deceleration phase should be considered (in addition to the geometry or severity of the stenosis) in decision whether the fluid simulations should be performed with or without the laminar flow assumption.

### 3.1.3. Assessment of the effect of the wall compliance on the haemodynamic parameters

Comparison of Figure 4A and B shows significant differences in the shape of the peak velocities in the middle of the rigid and compliant tubes. As the experimental setup and dimensions are almost the same for both, this difference could be mistakenly attributed to the wall movement of the compliant tube. However, the interpretation cannot be so straightforward. The main reason for such a great discrepancy is the non-negligible time shift between the pressure waves at the inlet and the outlet (*i.e.*, in case of the rigid tube the time shift is negligible) resulting in totally different pressure gradients along the tube compared to a rigid tube. In addition, at least two locations exist in case of the compliant tube, where almost stepwise changes in the impedance occur being responsible for high portions of the reflected waves. They are located

at the connections between the tested tube and the hydraulic circuit where the pressure sensors are embedded in metal (*i.e.,* nearly rigid) casings. This effect could be diminished by using materials with similar elastic modules for the whole circuit. Another source of the wave reflections and consequent oscillations, valves of the membrane pump, could be eliminated by using a peristaltic pump instead.
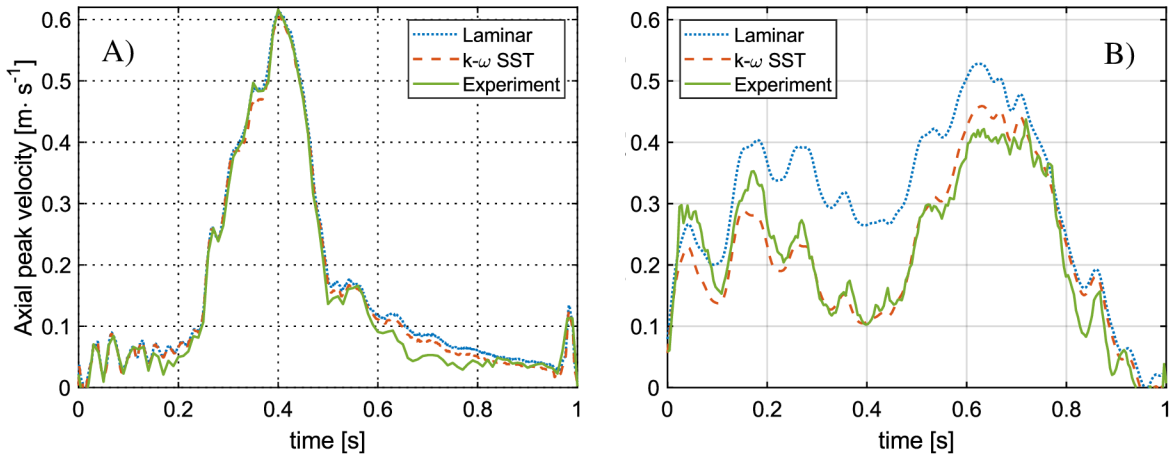


*Figure 4 Shape of the velocity waveforms in the middle of the tube (center of the cross section at the half-tube length). The rigid (A) and the compliant (B) tube.*

### 3.2. Comments on the main findings

The closed experimental circuit with its stepwise changes of stiffness is inconsistent with the arterial tree, which is characterized by a continuous distribution of parameters and terminates with a constant pressure in the capillary bed; thus it does not induce as many wave reflections as it was in the experimental circuit with its stepwise changes of stiffness. However, from the validation point of view, our conditions were harder (high frequency oscillations) than may occur in arterial blood flow. Therefore, the conclusions drawn on the basis of our simulations should be valid also for simulations of arterial flow, which can be, in addition, influenced also by the non-Newtonian blood properties and strain stiffening of the arterial wall.

In our study we worked with a rather well described tube (homogeneous, isotropic and hyperelastic) and also the BCs were recorded. However, for many computational studies which consider compliance of blood vessels (FSI analyses), such comprehensive inputs are not known. Number of the required inputs can be reduced by a lumped parameter model or structured tree model, usually used instead of the measured output pressure. For instance, in case of 3WK model used instead of the recorded transient pressure waveform at the outlet, only three unknown constants per each outlet have to be determined, *i.e.,* peripheral compliance, resistance and inertance. This approach was described in the chapter 2.4. Another option is to adopt representative BCs from the available literature [38–40] or from a validated 1D model of the whole arterial tree (1D [41] and/or 3D [42]). Regarding to these considerations, however, a synchronization between the input and outputs has to be done for correction of the time shift in the computational model because the time shift between the input and output BCs is PS and has significant influence on the flow. If not done, the pressure gradients along the domain can be highly different from their physiological values. It may result in a non-physiological flow in the simulations and, consequently, in incorrect results and conclusions.

# 4. Experimental and computational analysis of pulse wave propagation

## 4.1. Calculation of the PWV

The wave propagation phenomenon in an elastic tube can be mathematically described by Moens-Korteweg equation (4.1) [10]. This equation can be simplified into eq. (4.2), if compressibility of the fluid inside the tube is much lower than distensibility of the tube. For instance, compressibility modulus (*i.e.* bulk modulus) of water at 20°C $K$ is $2,03.10^9 [Pa]$ while incremental (or secant) modulus of elasticity $E_{inc}$ of a silicon tube used in experiment below equals to $4,55.10^6 [Pa]$ (see Figure 6), *i.e.* almost three orders lower. Moreover, the $E_{inc}$ is even lower (by an order) in case of large arteries.

$$PWV_{fluid+solid} = \sqrt{\frac{\frac{K}{\rho}}{1+\frac{K \cdot d}{E_{inc} \cdot s}}} \qquad (4.1)$$

$$PWV_{solid\ thin\ walled\ tube} = \sqrt{\frac{E_{inc} \cdot s}{\rho \cdot d}} \qquad (4.2)$$

$$PWV_{solid\ thick\ walled\ tube} = \sqrt{\frac{E_{inc} \cdot s}{\rho \cdot d \cdot (1-\mu^2)}} \qquad (4.3)$$

Here $\rho$ represents mass density of the fluid [kg·m$^{-3}$], $s$ and $d$ are thickness and inner diameter of a tube, respectively [m], $\mu$ Poisson's ratio [ - ].

Nevertheless, both of them represent an idealized wave velocity and are valid only under a number of simplifying assumptions for the tube: (i) thin-wall tube; (ii) it shows small deformations; (iii) it is filled with a perfect incompressible inviscid liquid; (iv) its wall material can be considered as Hookean; v) it has (straight) cylindrical shape. Deviation due to the first assumption can be lowered by using corrected Moens-Korteweg eq. (4.3), which can be found within Bergel´s doctoral thesis [43]; it incorporates Poisson's ratio of the tube. In practice, eq. (4.3) represents an effective simplification [11]. Despite of these limitations, the Moens-Korteweg formula is still frequently used to calculate arterial stiffness (from the PWV) or PWV [11]. Its utilization is reasonable because the main focus of these studies is evaluation of relative differences in PWV (e.g., between young and old, or systolic and diastolic conditions) rather than finding its true absolute value.

## 4.2. Experimental measurement of the PWV in a thick-walled hyperelastic tube

The experimental circuit is presented in Figure 5, dimensions of the compliant (silicone) tube are: L = 1.33 m; t = 0.003 m; Ød = 0.026 m. Two samples were cut from the tube to perform uniaxial tests with our in-house testing machine. One in the circumferal and one in the longitudinal direction. Every sample was tested twice, thus four uniaxial tests were performed in total (see Figure 6 – left). Because the tube was thick-walled, the circumferal sample preserves significantly a circular shape. Although a preload was used before the testing procedure, it was quite hard to find a threshold between bending and pure tensile loading of the sample. Hence, only two tests from the longitudinal sample were used to identify the material model. Moreover, the deformations of the tube from the pressure pulse are small (between ~ 1 ÷ 3%) and thus, $E_{inc}$ ~ 4.55 MPa (as an average from the slopes of two uniaxial tests, see Figure 6 - right) and $\mu$ = 0.5 (*i.e.* incompressible) were consider to fully describe the used Hookean

material model. Furthermore, the tube was regarded as isotropic, incompressible and homogeneous.
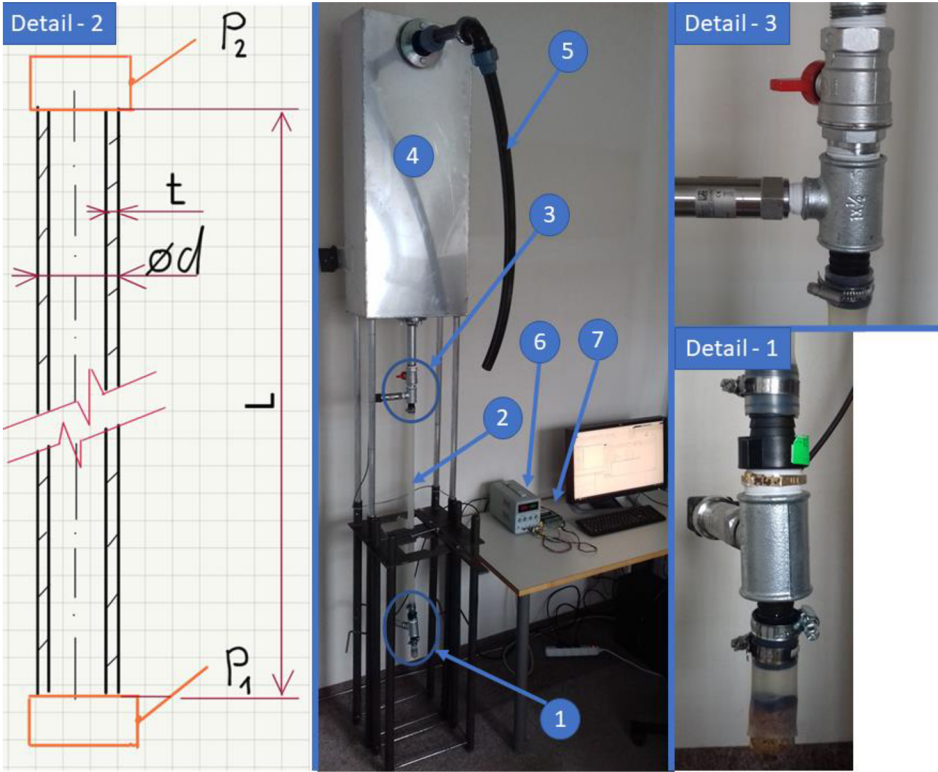


*Figure 5 Experimental circuit simulating pulse wave propagation. (1) - lower pressure sensor with a source of a pressure wave; (2) – test section (compliant tube); (3) – upper pressure sensor with a ball valve; (4) - output water reservoir; (5) – an overflow (6) – source of the AC current with a terminal block (7)*
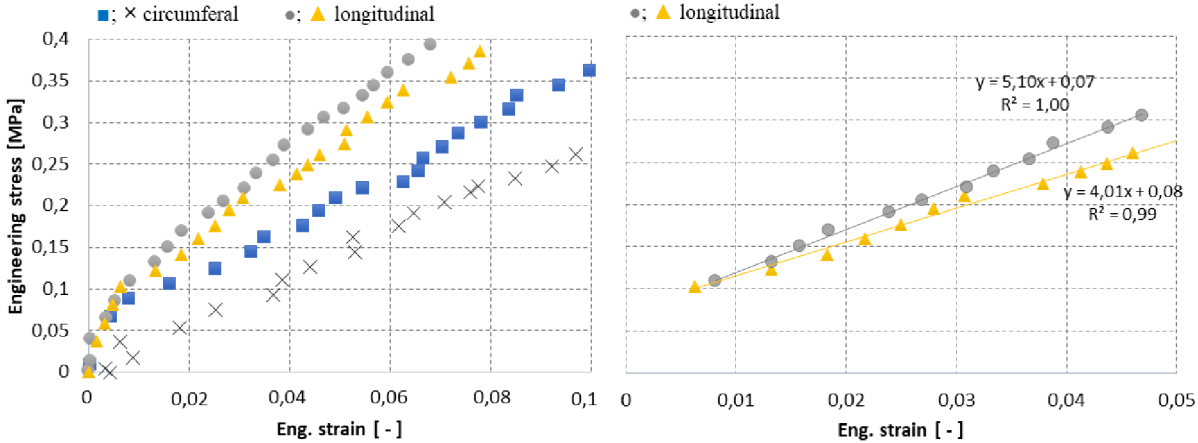


*Figure 6 Experimental data from four uniaxial tests (left figure). Zoomed results for longitudinal samples approximated with a straight line, the slope of which defines the Young's modulus (right figure).*

The working fluid of the circuit was water (at 20°C). Pressure sensors with sampling frequency of 200 Hz were located at the inlet and outlet of the test region (the measured tube). The pressure wave was actuated manually by pressing a short section of a tube right below the lower pressure sensor (see Figure 5, detail 1). The water reservoir (4) was connected to the circuit to set up the initial pressure in the circuit. Thus, a pressure difference between the lower and upper sensors

corresponds to 1.33 m column of water (*i.e.,* hydrostatic pressure of 0.0133 MPa), see Figure 7. To ensure that amplitude of the pressure pulse will not be significantly attenuated as it spreads toward the upper pressure sensor within the compliant tube, the ball valve was installed right behind the upper pressure sensor. This allowed me to control the amplitude of the pressure pulse.
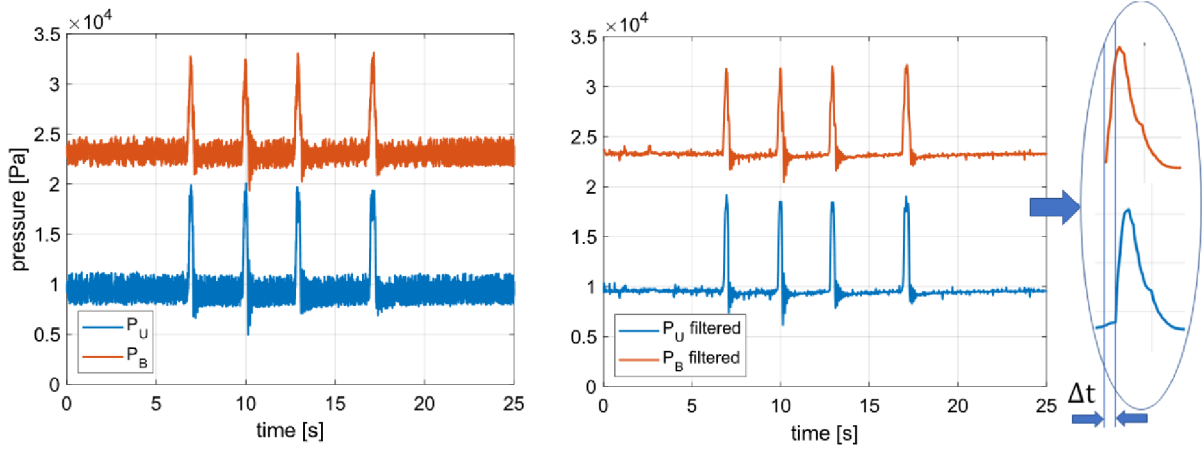


*Figure 7 Pressure pulses recorded from the lower (blue) and upper (orange) pressure sensors. The left side depicts a non - filtered data while filtered data are on the right.*

High frequency noise was filtered out by a low pass filter, consequently, the time-to-foot method was used to evaluate the time delay $\Delta t$ between the pressure waves from the bottom and upper pressure sensors (see Figure 7). As a result, the PWV ~ 35 m.s$^{-1}$ was calculated as a ratio between the length of the tube L and the time delay $\Delta t$.

## 4.3. Experimental validation of the PWV calculation

The FSI simulation of the PWV propagation along the thick-walled tube (made of silicone) was performed in ANSYS by coupling Fluent solver for the liquid phase with ANSYS Structural solver (based on Finite Element Method) for the solid phase. Due to axial symmetry, only a quarter of the test region (detail 2 in Figure 5) was considered in the computational model. Acceleration of gravity was not taken into consideration.
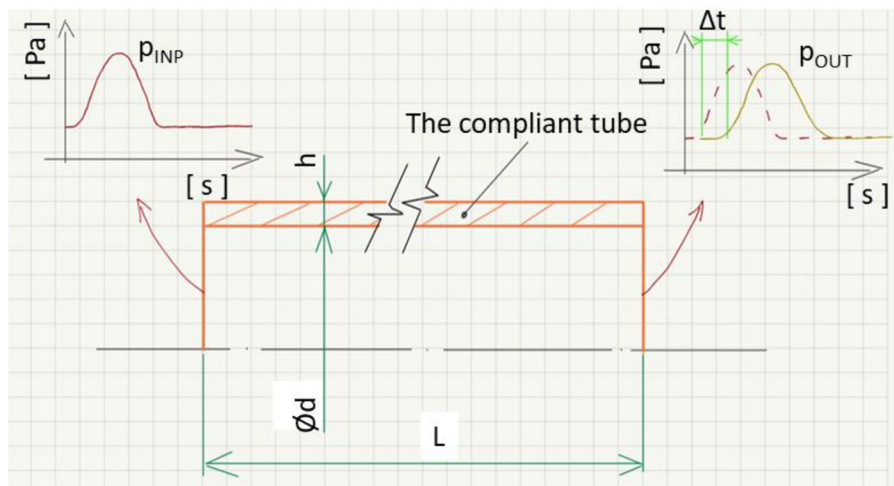


*Figure 8 Boundary conditions*

The idealized pressure waveforms represented by half-sine function were used as BCs at the inlet and outlet of the tube. Hovever, the BC at the pressure outlet was shifted behind the BC

at the pressure intlet by about $\Delta t = 0.0166$ s (see Figure 8). The time delay was calculated as a ratio of length of the tube L = 0.5 m to the PWV = 30.2 m· s$^{-1}$ where the PWV was figured out from eq. 4.3 (*i.e.* Moens-Korteweg eq. for a thick-walled tube). Time step size was set to 0.004 s, which was sufficient to achieve the required convergence criteria for residuals. These criteria were set to 10$^{-5}$ for velocity components and to 10$^{-4}$ for continuity.

A Hookean material model was used with E = 4.55 MPa and $\boldsymbol{\mu} = 0.5$ (*i.e.,* incompressible) because of small deformations of the tube; the process of identifying the used material model for the solid domain, was described in the above chapter. The P-U loop method (eq. 4.4 [44]) was adopted as an alternative and more precise approach (in comparison to Moens-Korteweg eqs.) for the PWV evaluation. It is worth to note that its fundamental equation (eq. 4.4) also does not consider viscous flow.

$$PWV = \frac{1}{\rho} \cdot \frac{dP}{dU} = \frac{1}{\rho} \cdot \Delta \qquad\qquad (4.4)$$

Where $\boldsymbol{\rho}$ represents density of the fluid [kg·m$^{-3}$], $\boldsymbol{dP}$ and $\boldsymbol{dU}$ are instantaneous increments of pressure [Pa] and velocity [m· s$^{-1}$] at the same location, respectively.

To obtain the PWV from FSI simulation, we have to extract the transient velocity and pressure profile from the same location within the tube. Thus the plot pressure versus velocity should be linear (if there are only forward waves present. Finally, the slope of the P-U line is equal to $\boldsymbol{\rho}$ *PWV*. Hence, it gives us the desired PWV = 34.7 m · s$^{-1}$ when divided by $\boldsymbol{\rho}$. Comparison of different computational approaches with experimental measurement can be seen in Table 1.

*Table 1 Comparison of multiple approaches of the PWV evaluation.*

| | Used method | | | |
|---|---|---|---|---|
| | *Time-to-foot method (experiment)* | *K-M basis* | *K-M correction for thick wall* | *P-U loop* |
| PWV [m/s] | 35.0 | 26.2 | 30.2 | 34.7 |
| Relative error [%] | - | -25.3 | -13.7 | -0.9 |

# 5. Analysis of influence of arterial geometry and flow waveform shape on hemodynamics in arteries

## 5.1. FSI parametric study of idealized arterial tree: effect of geometry

### 5.1.1. Brief Introduction

This chapter is dealing with 3D two-way FSI simulations of eighteen idealized and one PS geometries of human aortic tree with common iliac and renal arteries with different iliac angles and aorto-iliac ratios. The main goal is to evaluate the influence of these geometric changes on blood pressure in the AA. For instance, some FSI studies showed that increasing angle ω between iliac arteries at the bifurcation (see Figure 9), as found often in clinical practice, is associated with increased blood pressure (BP) and consequently stress within the abdominal aortic aneurysm (AAA) [38,40]. It has been shown experimentally that the ω angle increases and the area ratio AR (*i.e.* a sum of luminal cross sections of iliac arteries divided by the aortic luminal cross section) decreases with age [45,46], or could be modified through remodelling process due to haemodynamic changes caused by, for example, isolated common iliac artery aneurysms [47]. On the contrary, some experimental studies concluded that the effect of the bifurcation angle on the BP is small [46,48]. Regardless of the significance of these geometrical changes on the BP, the theory behind is that as the ω angle increases and the AR decreases, a higher-pressure wave reflection is induced at the bifurcation. The reflected wave may interfere with the forward pressure wave and result in a pressure increase in the AA where the elevated

systolic blood pressure (SBP) affects the aorta in the same way as in case of hypertension. Unfortunately, this effect is hardly detectable for clinicians because the BP is commonly measured in brachial artery [11,26,49]. Moreover, AAA is often associated with significant stenosis of iliac and/or femoral arteries and it is not clear whether iliac stenosis may contribute to AAA formation by increasing the BP in the AA. Also, it is still not clear whether the pressure in AA may be significantly elevated in a healthy aortic tree compared to other large arteries. Therefore we focused on this question and analyzed computationally the effect of both aorto-iliac angles and AR on predisposition to AAA development by quantifying their effect on the pressure and peak wall stress (PWS) in the AA during a heart cycle.

The following people participated in the work with me: Doc. Stanislav Polzer, PhD.; Ing. David Schwarz; Prof. Jiří Burša, PhD. The results of this computational study have been published in [50].
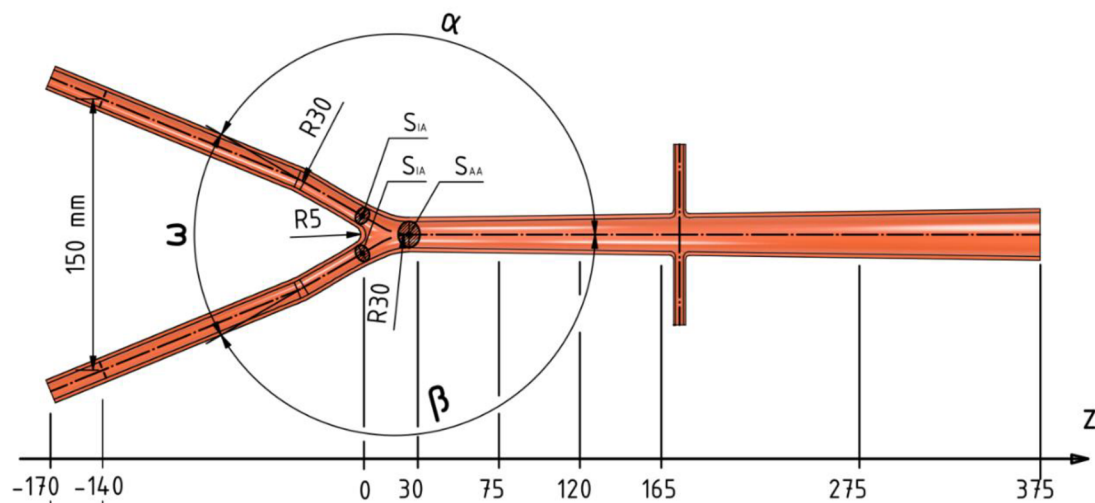


*Figure 9 Dimensions of the geometrical model of aorta and iliac arteries for basis geometry (upper). Angles $\alpha$ and $\beta$ change in the parametric analysis, z coordinate defining the position of sections origins at the bifurcation apex. Geometries are constructed in a way that ensures the same 150mm distance of iliac arteries at the 140 mm distance from the bifurcation apex. Cross sections of the abdominal aorta ($S_{AA}$) and iliac arteries ($S_{IA}$) were used in evaluation of the area ratio AR.*

### 5.1.2. Methods

*a) Geometry creation and mesh*

As regards to idealized geometries and meshes, a 3D finite element model was created with diameters (changing linearly along the aorta) and wall thicknesses of individual arteries set according to available literature to represent 60 years old men [51,52] who is typically in risk for AAA and/or atherosclerosis development (see Figure 9). Since this study consider elasticity of arteries (FSI analysis) and dimensions are measured *in-vivo* (*i.e.,* under diastolic/systolic BP), we have to solve inverse problem to find out undeformed dimensions. Thus, diameters and wall thicknesses were iteratively changed to minimise deviation of the calculated deformed dimensions from the *in-vivo* (deformed) values measured under diastolic and systolic BP and axial prestretch. The same diameter of both iliac arteries was chosen to set the AR ratio to 1 in the basis variant. This ratio is validated with *in-vivo* measurements (for a healthy older individuals) [41,53]. Since the AR variability is considerable [46] so we extended our study by adding geometries with different AR to simulate various degree of iliac stenosis or effect of aging. To cover an existing dispersion in geometry of aorto-iliac bifurcations, the shapes and

ranges of their parameters in both symmetric and asymmetric variants follow the shapes observed in elder patients (see Figure 10), both healthy and suffering from iliac artery aneurysm [47]. A different aorto-iliac geometries were created from the basis geometry (see Figure 9) by changing the angles $\alpha$ and $\beta$ and the AR. In accordance with anatomical reality, six combinations of different aorto-iliac angles between 30° and 150° were created and, for each of them, 3 variants with *AR* 1, 0.67 and 0.5.
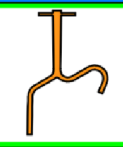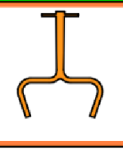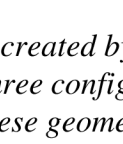


*Figure 10 Overview of six analysed bifurcation geometries created by varying angles $\boldsymbol{\alpha}$ and $\boldsymbol{\beta}$ of both iliacs for area ratio $\boldsymbol{AR} = \boldsymbol{1}$ with illustrations of three configurations. Three variants with $\boldsymbol{AR}$ = 1.0, 0.67 and 0.5 were created for each of these geometrical configurations.*

The PS geometry of a 53-years-old man with no arterial pathology in aorta was reconstructed from computed tomography–angiography (CT-A) using software Blender 2.91. (Blender Foundation, Netherlands), which floods the volume portions having the same Hounsfield units (HU) with finite elements. The aortic wall was assumed to be with constant thickness of 2 mm with local variation around bifurcations (necessary to prevent surface intersections). The PS geometry had AR of 1.05 and aorto-iliac angles of 148°/149° which is practically identical with our basis variant.

A mapped pure hexahedral meshes of the lumen (fluid) and the wall (solid) were generated for all geometries (*i.e.,* eighteen idealised and one PS) in Ansys ICEM CFD$^{\text{TM}}$. Detailed information regarding to mesh creation together with mesh sensitivity study can be found in [50].

### b) Used boundary conditions and constitutive models

A hyperelastic 3$^{\text{rd}}$ Yeoh model (isotropic incompressible) was used for the arterial wall defined by strain energy density function [54].

$$\Psi = \sum_{i=1}^{3} c_{i0}(I_1 - 3)^i \tag{5.1}$$

where $I_1$ is the 1$^{\text{st}}$ invariant of right Cauchy-Green deformation tensor and $c_{10}$=78 kPa, $c_{20}$=0 and $c_{30}$=27 kPa are material constants, corresponding to the elastic modulus of aorta at circumferential stretch of 1.15 and axial stretch of 1.08 of some 400 kPa which matches the values observed *in-vivo* [11]. The solid part was solved using FE software Ansys®. The applied axial pre-stretch of $\lambda_{ax}$= 1.08 represents a typical value for 60 years old patients [55]. An axial pre-stretch of $\lambda_{ax} = 1.16$ was prescribed in the same manner in renal arteries. In contrast, iliac arteries were not stretched but only fixed at their ends since it would cause their bending rather than stretching due to their curvature.

Blood was modelled as laminar flow of non-Newtonian liquid using Carreau model with viscosity being a function of shear rate $\dot{\gamma}$ as follows:

$$\eta = \eta_{inf} + (\eta_0 - \eta_{inf})[1 + \dot{\gamma}^2 t_0^2]^{\frac{n-1}{2}} \tag{5.2}$$

where n=0.3568 is a power law index, time constant $t_0 = 3.313\ s$, while $\eta_0 = 0.056\ Pa \cdot s$ and $\eta_{inf} = 0.0035\ Pa \cdot s$ refer to shear viscosities at zero and infinity strain rates, respectively [56]. The fluid part was solved using ANSYS FLUENT software. The velocity waveforms for the thoracic aorta inlet and renal outlet BCs together with the pressure waveform for iliac outlets were adopted from literature [12,57]. We have applied the same BCs for all cases because it is known that the flow through severely stenosed arteries (carotid or iliac) is kept constant up to 65 - 85% area reduction [58,59]. However, the input and output BCs are shifted against each other (see Figure 11) and this time delay differs between young and older individuals to consider their different AA wall stiffness. The P‑U loop method was used [44] for determination of the specific time delay. The method assumed that only forward waves are present which is true only for a phase right at the start of systole. Therefore, PWV was computed for particular parts of the arterial tree and shows an increasing trend towards the periphery (PWV ~ 7,3 and 8,8 m.s⁻¹ for infrarenal aorta and iliac artery, respectively), which is in line with normotensive older individuals [60]. After this adaptation we reached the pressure and velocity waveforms along the abdominal aorta within their physiological ranges [61]. It is noted the same analysis was done also for the PS geometry.
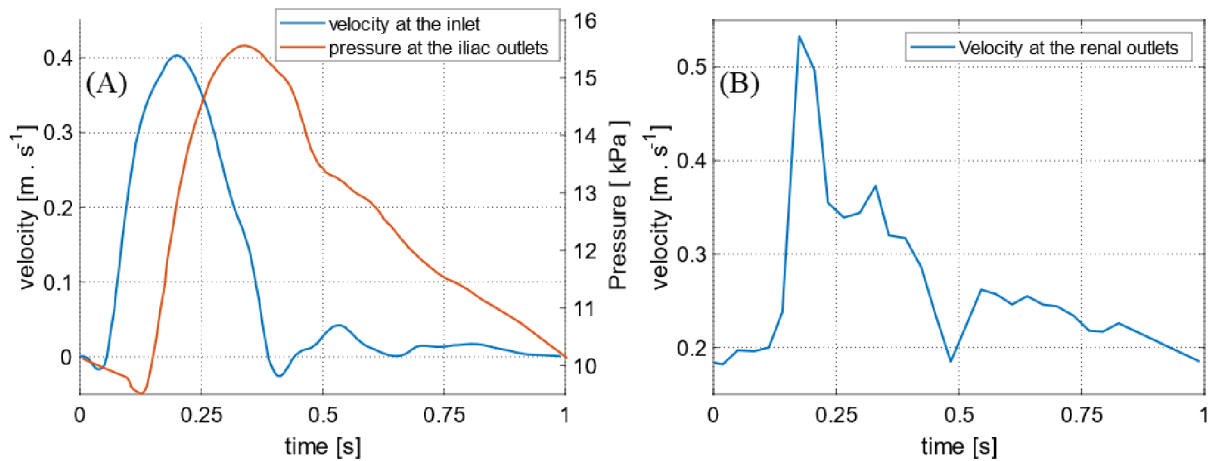


*Figure 11 (A) Pressure and velocity BCs adopted from a healthy young individual. (B) Mean velocity waveform at renal arteries as a result of averaging over six healthy individuals.*

Finally, the problem was modelled as transient with time step size set to $0.003\ s$ and 3 heart cycles were simulated; the data from the last cycle was considered as stable (see [50] for detailed fluid, solid and coupling setup).

### 5.1.3. Results

For each geometry, first principal stress (FPS) and pressures were recorded at three different locations along the AA (z = 30 mm, z = 75 mm and z = 120 mm). Relative change of circumferential strains was between 7.8% and 10.6% along the aorta, which is within the range reported in *in-vivo* measurements [51]. Further validation of the model via PWV, pressure and velocity waveforms can be found in [50].

#### a) Influence of bifurcation geometry on pressure and stresses

Pressure waves in the AA (z = 75 mm) are shown in for one extreme variant (150°/30°) and for the basis (150°/150° – see Figure 9) with $AR = 1$, 0.67 and 0.5. The impact of aorto-iliac angles

on the pressure wave and the SBP is negligible, in contrast to the more significant impact of the AR, increasing to + 0.67 kPa (*i.e.,* 4.1% of systolic and 10.2% of pulse pressure) and +1.22 kPa (*i.e.,* 7.5% of systolic and 18.8% of pulse pressure) for the ratios $AR = 0.67$ and $AR = 0.5$, respectively. The PS variant exhibited almost identical pressure waveforms as the basis (Figure 12, solid orange vs black dashed curve).

The resulting FPS in peak systole can be seen in Figure 13 for all the geometrical variants at three chosen positions along the AA. Again, variation along the AA is due to the changing dimensions while the results are practically independent of bifurcation angles (differences below 2%). Conversely, significant increase of FPS along the AA can be seen with decreased AR ratio. The PS variant exhibits FPS along the AA between 60 and 93 kPa (see Figure 14) which is close to values for the basis variant.
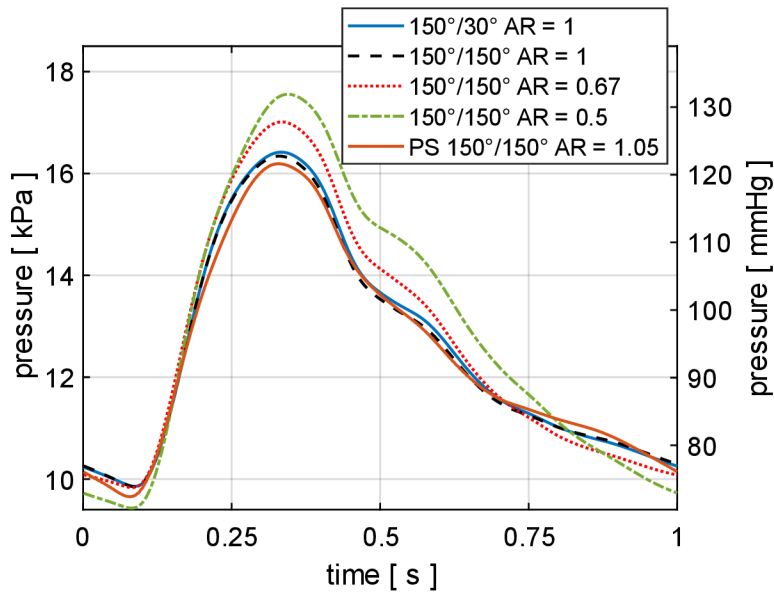


*Figure 12 Evolution of pressure in time in abdominal aorta (AA) (z = 75 mm) for an extreme combination of angles (150°/30°) and for the basis (150°/150°) with AR =*
*1, 0.67 and 0.5. Moreover, results from the patient-specific variant similar to the basis is depicted (orange curve).*



*Figure 13 Effect of aorto-iliac angles and ratio on peak wall stress at three locations along the AA. The grey rectangle represents the span of FPS along the AA in the PS variant.*

*Figure 14 Map of FP stresses along the AA in the PS variant. The PS variant exhibits FPS along the AA between 60 and 93 kPa which is close to values for the basis variant.*
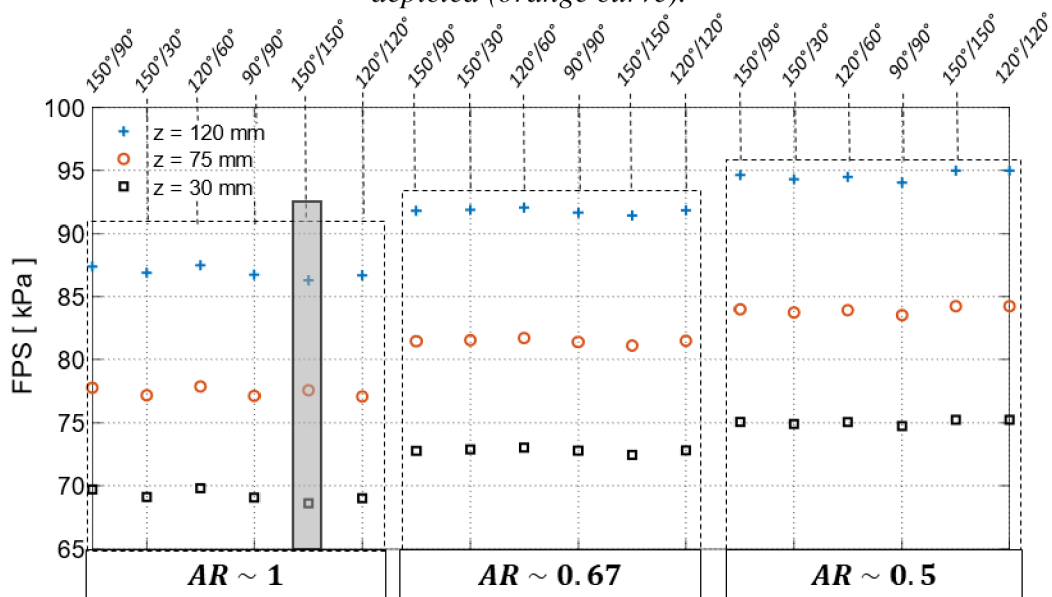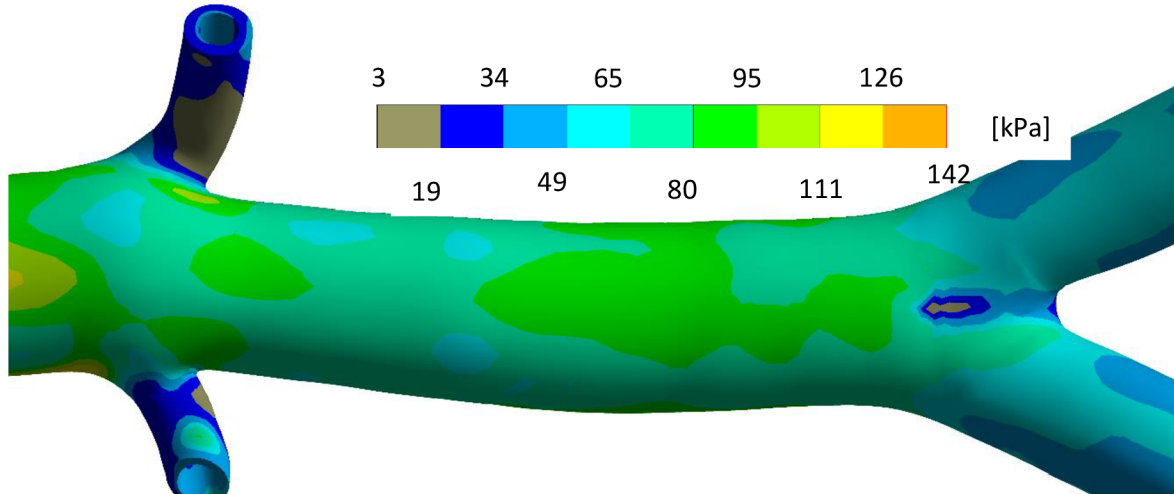
### 5.1.4. Discussion

In this study we have investigated the effect of aorto-iliac geometry variations on the peak pressure and FPS in AA via two-way weakly coupled FSI parametric analyses using (i) realistic constitutive models for both arterial wall and blood, (ii) realistic axial prestretch of AA and (iii) realistic (deformed) arterial wall thicknesses and diameters. The idealized geometries were validated with a PS geometry confirming that the simplification necessary for parametric analyses did not affect the drawn conclusions and their applicability. Moreover, we have focused on a proper time shift between fluid phase boundary conditions which is not common in these analyses [38,40].

#### a) Aorto-iliac angles do not affect BP in AA

We have shown the effect of aorto-iliac angle on SBP and FPS is negligible across wide variety of considered geometries (see Figure 13). Our results are in agreement with previous experimental studies [46,48] while they seem to be in contradiction to previous computational studies [38,40] showing some increase in SBP and FPS in the wall. However, those studies analyzed an AA with aneurysm while we focused on stresses and BP in a non-dilated AA. Moreover, the discrepancy could be related to different boundary conditions for the solid phase. The mentioned studies have not applied any axial pre-stretch, thus the axial movement at the bifurcation was hardly constrained, especially in the cases with higher iliac angles. This resulted in higher PWS at the apex and on the sides of the bifurcation. Our model with axial pre-stretch applied on the AA does not show this dependence and we believe to be closer to reality.

Another substantial difference is the time shift between BCs applied in our study. We have shown that unrealistic BC shifts lead to an increase or decrease of BP in the AA as shown in [50]. Unfortunately, studies [38,40] did not synchronized BCs which may explain the different conclusions.

#### b) Decrease of iliac diameters increases BP in AA

Contrary to the negligible effect of the aorto-iliac angle we observed significant dependence of BP on iliac diameters (*i.e.,* the AR ratio). In our simulations, the decreased dimensions of iliac arteries increase their resistance, which results in a higher pressure along the AA due to higher and earlier wave reflection. Thus the 50% iliac stenosis leads to FPS increase in the AA of some

8% (see Figure 13). Although this is certainly not enough to cause any immediate problems, its cumulative effect with other risk factors may accelerate a potential development of AAA. Moreover, for development of vascular diseases, not only the SBP but also pressure pulsations might be important and their relative magnitude increased by 19%. That would be in line with clinical observations showing the veterans with lower limb amputation (*i.e.,* occlusion of one iliac artery) have much higher prevalence of AAA [62]. Occlusion of one femoral artery due to amputation is similar to 50% stenosis of both iliac arteries simulated here. Comparison to other studies [38,40] is not possible because they did not vary the AR.

Several limitations should be considered when interpreting our results and we discuss it properly in [50].

## 5.2. CFD simulations on patient-specific carotid arteries: effect of flow waveform

The main goal of this computational study is to assess the influence of young versus old archetypal flow waveforms on hemodynamical conditions in PS human carotid artery bifurcation geometries. Based on the research performed, we pointed out that the shape of the flow waveform changes with age of the individual (similarly as arterial hypertension) and is closely related to stiffness of his/her arteries. It was also shown that physical exercising, healthy lifestyle or antihypertensive treatment can shift the shape of the flow wave close to a young and healthy one via lowering the arterial and peripheral stiffness. Taking these pieces together, a new mechanism how these factors attenuate the risk of atherosclerosis is shown below.

I am working on a manuscript to be submitted to an IF journal at the end of the august 2023. I formulated its basic idea and concept and did also most of the research, simulations, and methodology proposal. Thus, I will be the first author of the manuscript. Nevertheless, since it is a greatly interdisciplinary problem, many other colleagues were involved: Ing. Petr Hájek, PhD.; MUDr. Tomáš Křivka; MUDr. Tomáš Novotný, PhD; Ing. Jiří Kohút; Ing. Martin Formánek and Prof. Jiří Burša, PhD.

### 5.2.1. Introduction

Many similarities can be seen between the blood flow dynamics within subjects with the age-related elevation of arterial stiffness [63] and those with arterial hypertension [64]. In addition, the archetypal flow waveform shapes for young and old subjects can be found for the human carotid artery in the literature [63,65,66]. The most pronounced differences occur in presence of late systolic peak (see Figure 15, point $V_2$) which probably arise from the earlier return of the reflected waves (compared to young ones) from local upper-body sites and their interaction with later wave reflections returning from the opposite direction from sites in the lower part of the body in case of old waveform [11,63]. Their earlier return is probably the result of increase in PWV due to increase in arterial stiffness with age. Since arterial stiffness can be lowered through long-term application of all five basic groups of antihypertensives (angiotensin receptor blockers–ARB, calcium channel blockers–CCB, and angiotensin-converting enzyme inhibitors–ACEi, beta-blockers, and diuretics) [26,49,67,68], possible benefits of such medical therapy could be not only in lowering the BP and peripheral resistance as mentioned in literature [26,49,68,69] but also in improving other hemodynamic conditions such as WSS.

Nevertheless, I and my co-workers have found only one comprehensive hemodynamic analysis of this phenomenon [70]. This numerical study reported negligible hemodynamic differences between representative young and elderly waveforms for the human carotid artery. Although the conclusions stated in [70] were formulated on the basis of nine PS geometrical models, their inter-subject variability was quite low. Moreover, they used archetypal waveform referenced as

young from [71] where 17 young, normal volunteers were measured, despite of existence of a more statistically significant study [66], where the authors recorded and analysed 3560 cardiac cycles in total (with the same number of volunteers) to assess inter- and intra-subject variability. Above that, we decided to extract the flow waveform from the latter study for two more reasons: (i) the instantaneous velocities were measured with temporal resolution three times shorter (*i.e.,* of ~ 12 ms for the [66] while ~ 36 ms in case of the [71]); (ii) the flow archetypal waveform are in line with that reported in [65] where also detailed reasoning of such shape is introduced on the basis of aortic valve closure and reflected waves from the upper and lower part of the body.
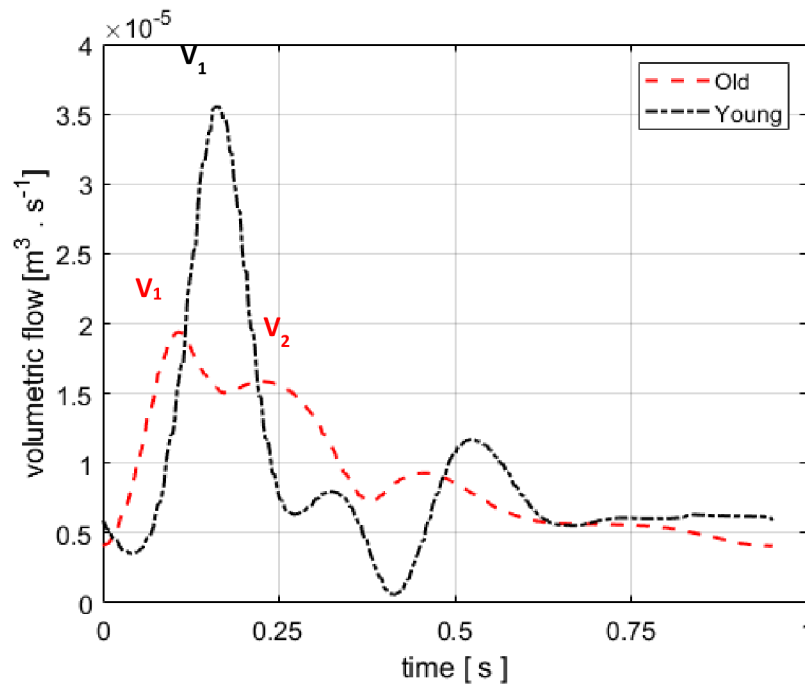


*Figure 15 Comparison of the young and old flow waveforms (black and red curves, respectively). The most pronounced difference occurs in presence of late systolic peak (point V2) in the old waveform while only one systolic peak exists within the young flow waveform.*

In the current study, we aim to assess the hypothesis stated in [70], that the differences between young and elderly archetypal waveforms have a negligible impact on hemodynamics and thus on elevated risk of the atherosclerosis development. This is done via 3D transient CFD analysis of five PS geometries of human carotid arteries with archetypal flow waveform shapes corresponding to healthy young and elderly individuals extracted from the two most relevant *in-vivo* studies [63,66]. The geometries have been selected with emphasis on a pronounced inter-subject variability and thus we believe our results can further strengthen or dispute the conclusions in [70]. Moreover, this is the first study trying to quantify the influence of hypertension or true aging process on hemodynamics in a carotid artery and to elucidate possible mechanisms for secondary benefits of the anti-hypertensive drugs therapy within these groups.

### 5.2.2. Methods

#### a) Lumen geometry extraction

The carotid arteries with characteristic shapes of the bifurcation were chosen from a set of 89 patients supplied from St. Anne´s University Hospital Brno deposit. Five healthy subjects (61±27 years old) without known coronary, cerebral, or peripheral artery disease and without

carotid artery stenosis were selected for the current study, with an emphasis on heterogeneous carotid anatomy such as diverse bifurcation geometry (angle, curvature). Typical provided raw data originated from CT-A scans with the in-plane resolution of 2.048 pixels per mm and with the slice spacing of 0.45 mm. Thresholding and segmentation were done manually in the open-source ImageJ software (https://imagej.net/software/fiji/downloads) and the proprietary licensed Medical 3D Image modeling software [72], respectively. Subsequently, the obtained stereolithography (STL) models were smoothed and regularized in the GOM Inspect software (https://www.gom.com/en/products/zeiss-quality-suite/gom-inspect-pro) with the surface tolerance below 0.2 mm, which lied safely below the CT-A scan resolution. The STL meshes were interpolated by the non-uniform rational base spline (NURBS) surfaces in Catia V5R21. The final surface body of the carotid artery was equipped with a circular inlet situated one millimeter below the caudal plane of the artery. The inlet is located at least in a distance equal five times the diameter of the artery upstream to carotid bifurcation. Outlets from the internal (ICA) and external carotid artery (ECA) were cut just before a next bifurcation.

*b) CFD simulations and boundary conditions*

Five finite volume models of PS geometries of human carotid bifurcations were created based on CT-A scans. Laminar blood flow was modelled in Ansys® Fluent® using Carreau model of non-Newtonian incompressible liquid with viscosity being a function of shear rate $\dot{\gamma}$ as presented in chapter 5.1.2.

To avoid an unrealistic piston profile at the inlet, an instantaneous 3D parabolic velocity profile was computed from volumetric flow BC and implemented (via user-defined function - UDF) in Ansys Fluent. In total, two different (old [63] and young [66]) archetypal flow waveforms were used. The mean velocity waveform was obtained from the flow waveform and inserted into the analytical solution of a parabolic profile. For both young and older waveforms, the periods were set to 65 bpm and the cycle-averaged flow rate for the CCA was allometrically scaled by the ratio of the CCA area to the average CCA area over all the subjects, as recommended in [73]. Moreover, young flow waveform was scaled by factor 1.08 to ensure the same cycle-average flow as the older one.

The 3WK was imposed at each outlet via UDF to create complete 3D-0D model of the carotid artery (3D model) and its periphery (0D model). To estimate its parameters efficiently, a lumped-parameter (*i.e.,* 0D only) model of the whole carotid arterial tree (from CCA to periphery) was created in MATLAB® Simulink® 2022b (the Simulink file with the lumped-parameter model of carotid artery can be found in the supplementary material). The lumped-parameter model consists of:

- o two 3WKs connected to the ICA and ECA outlets representing the periphery (see Figure 16 - blue box). Its suitability for such purpose was proved elsewhere [31,33,74].
- o three 2WKs representing each segment of carotid artery (*i.e.,* CCA, ECA and ICA). Each 2WK consists of one resistance term ($R_{CC}$, $R_{IC}$, $R_{EC}$) and one inductance term ($L_{CC}$, $L_{IC}$, $L_{EC}$) connected in a serio-parallel manner (see Figure 16 – red boxes). Since we are interested in the older patients having commonly stiffer arteries, the compliances C of individual segments were not considered.

The initial values of the resistance R and inductance L (*i.e.,* 2WKs) for the CCA, ICA and ECA segments with length $l$ and inner radius $R_0$ were computed from equations (5.3 and 5.4) based on averaged dimensions and steady and Newtonian flow assumptions [31]:

$$R = \frac{8l\eta}{\pi R_0^4} \qquad\qquad\qquad\qquad [\text{ N s m}^{-5}] \qquad\qquad (5.3)$$

*i.e.,* Hagen-Poiseuille eq. where $\eta$ is dynamic viscosity.

$$L = \frac{\rho l}{\pi R_0^2} \qquad\qquad\qquad\qquad [\text{ kg m}^{-4}] \qquad\qquad (5.4)$$

where $\rho$ represents blood density.

Then, the initial values for the periphery (*i.e.,* 3WK) were extracted from [31].
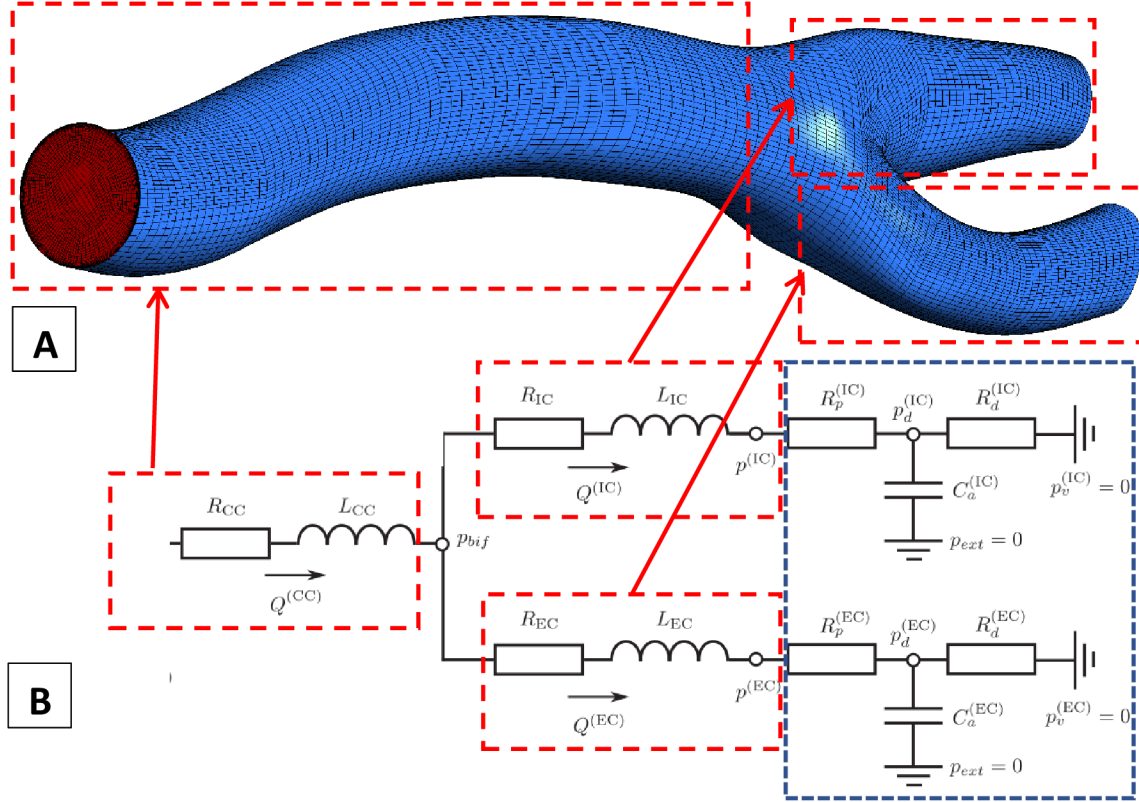


*Figure 16 (A) A 3D model of patient-specific carotid artery and (B) its corresponding reduced-order model representation (Modified from [31])*

Since an initial parameter guess is known, the parameter estimation procedure was used to obtain an estimate of the 3WK parameters of the periphery while the other parameters were fixed. The flow waveform at the CCA [63] was used as input to the lumped model while the flow waveforms measurements at the ECA and ICA outlets were used as reference signals. The unknown parameters (*i.e.,* $R_p^{IC}$; $R_p^{EC}$; $R_d^{IC}$; $R_d^{EC}$; $C_a^{IC}$; $C_a^{EC}$) were estimated by minimizing the error between outputs from the model and the reference signals via nonlinear least-square method. This system of differential and algebraic equations (DAE) was implemented into Simulink environment. The solution of these equations was obtained from Simscape DAE solver with a default configuration.

Thereafter, the parameter estimates ($R_p^{IC}$; $R_p^{EC}$; $R_d^{IC}$; $R_d^{EC}$; $C_a^{IC}$; $C_a^{EC}$) were used to start the 3D-0D (multiscale) simulation. Only two iteration cycles based on the results from 3D-0D simulation were needed to satisfy the root-mean-square-error < $3.5e^{-7}$ between the reference signals (*i.e.,* measurements) and the 3D-0D model (see Figure 17). However, it can be anticipated that more iterations will be needed as the number of outlets increases.
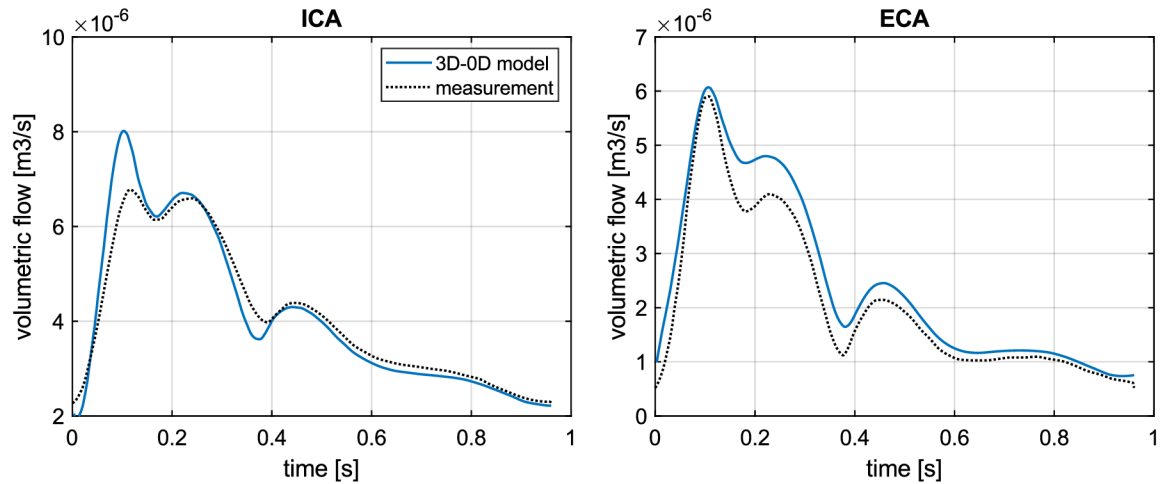
*Figure 17 Comparison of the reference signals (measurements) and flow waveforms from 3D-0D simulation at the outlets from internal (left) and external (right) carotid artery after second (final) iteration cycle. Root-mean-square-errors are < 3.5e$^{-7}$.*

### c)   Mesh and model validation

A mapped pure hexahedral mesh of the lumen was generated in Ansys ICEM CFD$^{TM}$ (see Figure 18). Around 48 elements across the CCA diameter were used with their axial length of ~ 0.8 mm and radial size changing from ~ 0.015 mm to ~ 0.14 mm between the wall and the central region (see Figure 18B) to capture the steep changes in the boundary layer. For a mesh sensitivity study, this basic variant with 300k elements was compared with a mesh refined to 1000k; the velocity profiles matched well and differences remained below 2% for most of the cardiac cycle. The computational domain was discretized in time with a step size of 0.003 s. To meet the required convergence criteria, the solver iterated until the residuals were less than 10$^{-4}$ for continuity equation and 10$^{-6}$ for velocity components at the end of each time step. As the quantitative differences between the 2$^{nd}$ and 3$^{rd}$ period were < 1%, the 2$^{nd}$ cycle was considered as stabilized. It is worth to note that mesh sensitivity study was performed with $k$ - $\omega$ SST model of turbulence with low-$RE$ corrections to verify laminar flow assumption. Some minor changes between $k$ - $\omega$ SST and laminar model were observed. Despite of this, we chose laminar model since the main purpose of this study is primarily a relative comparison between two archetypal flow waveforms.
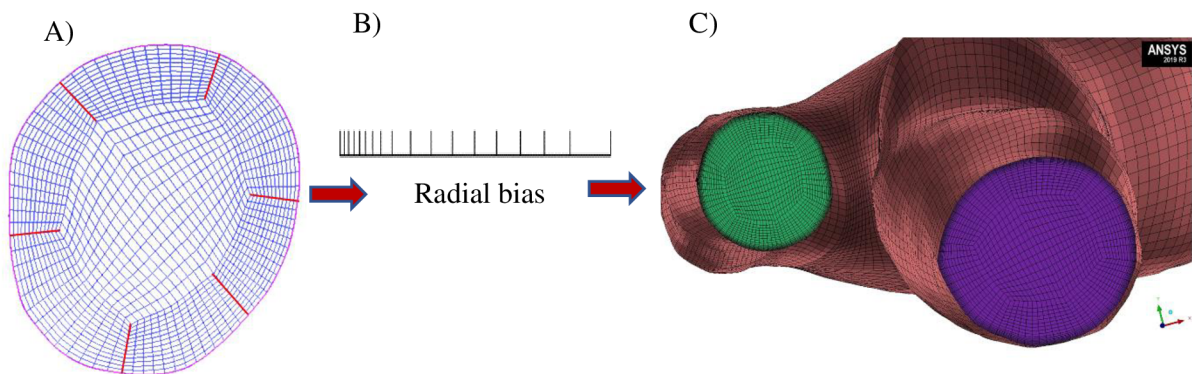


*Figure 18 Pre-meshing and its feature for radial discretization. A) Hexahedral mesh of the outlet from ICA. B) Changes in element size with distance from the wall along each radial edge (red lines in fig. A). C) – Final mesh of the PS carotid artery respecting linear law discretization in radial direction.*

A time-averaged wall shear stress (TAWSS) together with a relative residence time (RRT) were used as hemodynamic indicators for the risk of atherosclerosis development. The former has high sensitivity and low positive predictive value (PPV) while the latter has the opposite [75]. Regions are classified as atheroprone (from a merely fluid dynamic point of view) if TAWSS is < 0.48 Pa and RRT > 2.9 Pa$^{-1}$ [70]. TAWSS and RRT were derived from the calculated wall shear stress field using MATLAB® and Ansys CFD Post$^{TM}$. In order to calculate RRT, oscillatory shear stress (OSI) was defined. All of these parameters are defined according to [75].

### 5.2.3. Results

Results were extracted from the 2$^{nd}$ cycle of the transient 3D CFD simulations in which a stabilized cyclic response was reached. They show a significant reduction of the TAWSS risk areas (*i.e.,* areas showing TAWSS below its threshold value of 0.48 Pa) for the young archetypal waveform (see Figure 19 and Table 2). Moreover, TAWSS risk areas are totally missing in the patients 2 and 5 thanks to the favourable influence of the young waveform (see Table 2, second row). The RRT risk areas (*i.e.,* areas with RRT above the threshold value 2.9 Pa$^{-1}$) are not depicted while they correlate well with the TAWSS risk areas. Only their quantitative evaluation can be found in the Table 2. When RRT risk areas from old and young cases are compared, only minor changes with unclear trend can be observed.
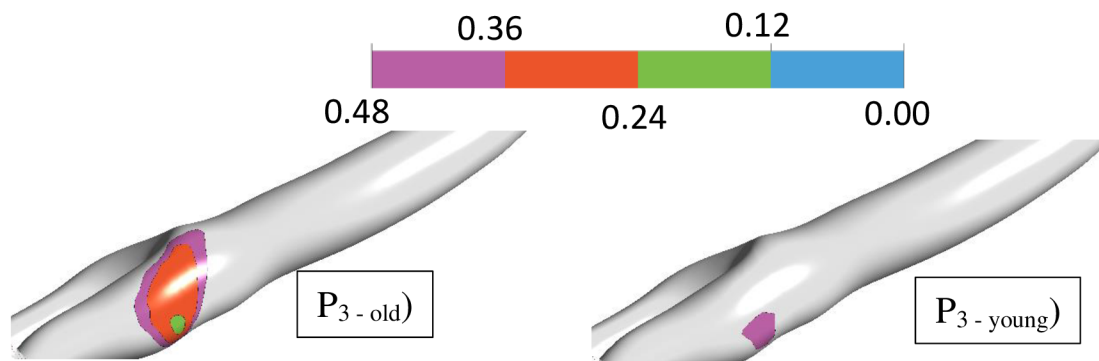


*Figure 19 Maps of the time-averaged wall shear stress for patient 3. Results for the old (left) vs young (right) archetypal flow waveforms and in top views show significant reduction of the risk factor for the young flow wave form. One representative geometry was selected for qualitative comparison.*

*Table 2 Δ₁ represents a relative change of the TAWSS and RRT risk areas due to application of the young flow waveform against the old one.*

| | TAWSS risk area [ m$^2$ ] | | $\Delta_1$ [ - ] | RRT risk area [ m$^2$ ] | | $\Delta_1$ [ - ] |
|---|---|---|---|---|---|---|
| | Old | Young | | Old | Young | |
| P1 | 2,17E-05 | 1,99E-06 | -91% | 2,18E-05 | 2,59E-05 | 19% |
| P2 | 4,43E-05 | 0,00E+00 | -100% | 4,53E-05 | 4,32E-05 | -5% |
| P3 | 8,67E-05 | 8,78E-06 | -90% | 8,00E-05 | 7,12E-05 | -11% |
| P4 | 1,11E-04 | 3,36E-05 | -70% | 1,08E-04 | 9,65E-05 | -11% |
| P5 | 1,88E-05 | 0,00E+00 | -100% | 2,76E-05 | 2,13E-05 | -23% |

To compare our results with clinical outcomes from [76][77], we have evaluated that the area-averaged TAWSS decreases on the straight CCA segment if the young flow waveform is used instead of the old one. Moreover, we added similar comparison in the risk areas (*i.e.,* areas where RRT is above 2.9 Pa$^{-1}$). For the old flow waveform, the area-averaged TAWSS over

straight CCA segments is by 11 – 18% lower (*i.e.,* more risky) than for the young waveform while these percentage of decrease is 2.5 – 4.5 times higher in the risk areas (see Table 3).

*Table 3 $\Delta_2$ represents a relative change of area-averaged TAWSS due to application of the old flow waveform against the young one.*

| | straight CCA segment | | | risk area | | |
|---|---|---|---|---|---|---|
| | area-averaged TAWSS [ Pa ] | | | | | |
| | Old | Young | $\Delta_2$ [ - ] | Old | Young | $\Delta_2$ [ - ] |
| **P1** | 1,73 | 1,98 | -13% | 0,51 | 0,74 | -32% |
| **P2** | 1,75 | 2,05 | -15% | 0,71 | 1,19 | -41% |
| **P3** | 1,19 | 1,45 | -18% | 0,44 | 0,77 | -43% |
| **P4** | 1,11 | 1,28 | -13% | 0,39 | 0,64 | -39% |
| **P5** | 1,14 | 1,28 | -11% | 0,64 | 1,27 | -50% |

### 5.2.4. Discussion

Our results are in contrast to those reported in the only one existing study on this topic [70]. They reported negligible hemodynamic differences between young and older waveforms in nine carotid arteries used in their simulations. Nevertheless, our results are in agreement with clinical studies [76,77] which reported a significant decrease ( ~ 15% within a 12-years period and ~ 34 – 46% within a 60-years period, respectively) in the area-averaged TAWSS within neck vessels with age. We used young and older waveforms corresponding to 28±3 and 68±8 years old subjects, respectively, and our results showing the area-averaged TAWSS are lowered by 13 – 18% (see Table 3), for the older flow waveform falling close to observed range. It is worth noting that the lower decrease in our simulations is reasonable due to the fact, that we fixed the trend of other potential contributors to the TAWSS decrease observed in those *in-vivo* studies (i.e., luminal diameter, arterial stiffness and SBP increase while blood flow decrease with age). In addition, we have shown that the area averaged TAWSS decrease is much more pronounced in the risk areas in comparison to the straight CCA artery segment (see Table 3). Nevertheless, some discrepancies regarding the cause of the area averaged TAWSS decrease have to be discussed here. Within the clinical studies [76,77] many other factors do also change, making thus almost impossible to distinct the most important contributor to the TAWSS decrease. Notwithstanding, both the clinical studies point out the main contributors are probably the increased luminal diameter together with the decreasing blood flow. The former study with older patients is longitudinal (i.e., the same patients are evaluated after 12 years from the baseline measurement) and includes 48 patients only. Although their data show very marked increase in arterial stiffness during this 12-years follow-up period (+74.5% in women and +28% in men), the authors do not discuss its potential effect on the TAWSS decrease. The latter study has 301 patients and investigates the cross-sectional area changes with the age ranging between 18-84 years. The authors are somewhat less confident in this conclusion because the most pronounced drop in TAWSS does not correspond with a significant drop in flow but do correspond with increase in luminal diameter and SBP. Unfortunately, arterial stiffness is not evaluated here. However, it is broadly recognized, that the SBP correlates positively very well with arterial stiffness. Thus, both studies show significant increases in arterial stiffness and SBP followed by a decrease in TAWSS. The results of our computational study shed some light on the potential contribution of the elevated arterial stiffness or SBP to the TAWSS decrease with arterial aging, when all the parameters were kept identical except for the flow waveform

boundary condition (which represents increased arterial stiffness). Moreover, it shows that the area-averaged TAWSS decrease with the old flow waveform is much more pronounced when evaluated at risk areas instead of the straight CCA segments as commonly done in clinical studies (see Table 3).

In conclusion, it seems that the significant decrease (especially in the risk areas) of the TAWSS related to the old archetypal flow waveform may increase the risk of future atherosclerosis development. This important mechanism accelerating the atherosclerotic process may be mitigated by antihypertensives or regular aerobic exercise. Both reduce the wall stiffness, transforming thus the flow waveform to a younger one and consequently decelerating the atherosclerotic process through increase of the TAWSS and decrease of the RRT in the risk regions.

- *Potential Limitations*

Although it is well reported that aging influences the flow waveform analogous to the arterial hypertension mainly due to the elevated arterial stiffness and to the consequent early return of the reflected waves, we have not found any *in-vivo* study related to the influence of antihypertensives on the flow waveform. Due to paucity of the data on the effect of antihypertensives on blood flow in carotid artery, an assumption was stated that antihypertensives shift the shape of the flow waveform typical for older or hypertensive individuals towards the young one. Although such assumption might be too optimistic, our results contribute to the strong evidence that the hypertension is a leading risk factor for major CVDs, such as heart attack, stroke, chronic kidney disease, heart failure, cognitive impairment and [11,78]. These late complications of hypertension are closely associated with the process of atherosclerosis. Even though this process is still generally poorly understood, an important mechanism playing a role in its development seems to be endothelial dysfunction [79]. Wall shear stress related to vascular hemodynamics is proven to affect endothelial dysfunction [80]. Antihypertensive drugs may improve or restore endothelial function through multiple mechanisms (direct effect on endothelial cells, hemodynamic effects, wall shear stress changes, etc.) [81]. The exact mechanisms, however, need to be elucidated in the future.

Further enlargement of this study will be possible as soon as some representative flow waveforms at the carotid artery will be available on patients with hypertension before and after a medical treatment reducing the blood flow resistance and arterial stiffness.

# 6. Conclusions

- Creation of a credible computational model of pulsatile blood flow in arteries, including its BCs, and its validation with experiments.

*The results of the computational and experimental study have been published in [35]. I am the first author, and this work fulfils the first goal completely. On the top of that, a very high-quality master thesis was the output which laid down the foundation for the long-term enriching cooperation with Ing. Jiří Kohút and fluid engineering department.*

- Design and creation of an experimental circuit simulating pulse wave propagation (PWV) in a compliant tube.

*The experimental circuit was designed and created; however, any publication or conference contribution have not been published so far. For this reason, the methodology is briefly described in section 3. Nevertheless, this circuit together with the related computational methodology for PWV evaluation have been implemented into the biomechanical lectures. Moreover, the proposed circuit serves as a basis for consequent projects focused on the peristaltic pump. It is worth to note that these projects established new cooperations (doc. MUDr. Pavel Suk, PhD., Ing. Martin Formánek and his modified doctoral topic in mechatronics).*

- Exploitation of the created model for FSI analyses of human aortic tree and evaluation of impact of some of its geometrical parameters on the risk of development of aneurysms and atheromas in critical regions.

*The results of the computational study regarding FSI analyses of human aortic tree have been published in IF journal Medical Engineering & Physics [50]. This study showed an insignificant impact of aorto-iliac angle on the haemodynamic parameters but a significant increase of aortic pressure and consequently of AAA risk for lower area ratio (i.e., a sum of luminal cross sections of iliac arteries divided by the aortic luminal cross section). I am the first author, and this work fulfills the third goal completely.*

- Creation of a 3D CFD PS model of human carotid arteries with lumped parameters BCs. Analysis of influence of diastolic phase length on hemodynamic parameters.

*This is the last, and probably the most interdisciplinary goal. Many surgeons from Saint Anne hospital were involved together with other colleagues from Brno University of Technology. Now, I am working on the manuscript which is planned to be submitted to an IF journal at the end of the august 2023. The only difference between the final manuscript and the work described here is a number of PS geometries. In the final manuscript is it planned to include 10 geometries, so far we have only 5. The main goal of this computational study was to assess the influence of young versus old archetypal flow waveforms on hemodynamical conditions in PS human carotid artery bifurcation geometries. Among broadly reported SBP-lowering effect of five basic group of antihypertensives (ACEi, ARB, CCB, beta-blockers, and diuretics), we hypotheses (based on literature review and high-fidelity computational simulations) their potential secondary benefit. Their favorable effect lies in significant increase of TAWSS as a result of decreasing the arterial stiffness and relating PWV. Such TAWSS increase (especially in atheroprone region, see Table 3) is probably one of the possible mechanisms how the risk of atherosclerosis is attenuated. Since it is not published yet, the actual state (including methodology, partial results and discussion) is described in section 5.2 in detail..*

# 7. References

[1]     J.C. Riley, Estimates of regional and global life expectancy, 1800-2001, Popul. Dev. Rev. 31 (2005) 537–543. https://doi.org/10.1111/j.1728-4457.2005.00083.x.

[2]     S.L. Murphy, J. Xu, K.D. Kochanek, E. Arias, B. Tejada-Vera, Deaths: Final Data for 2018, Natl. Vital Stat. Reports. 69 (2021).

[3]     B. Keisler, C. Carter, Abdominal aortic aneurysm, Am. Fam. Physician. 91 (2015) 538–543.

[4]     S.P. Glasser, A.P. Selwyn, P. Ganz, Atherosclerosis: Risk factors and the vascular endothelium, Am. Heart J. 131 (1996) 379–384. https://doi.org/10.1016/S0002-8703(96)90370-1.

[5]     K.C. Kent, R.M. Zwolak, N.N. Egorova, T.S. Riles, A. Manganaro, A.J. Moskowitz, A.C. Gelijns, G. Greco, Analysis of risk factors for abdominal aortic aneurysm in a cohort of more than 3 million individuals, J. Vasc. Surg. 52 (2010) 539–548. https://doi.org/10.1016/j.jvs.2010.05.090.

[6]     H. Sillesen, E. Falk, Why not screen for subclinical atherosclerosis?, Lancet. 378 (2011) 645–646. https://doi.org/10.1016/S0140-6736(11)60059-7.

[7]     C. Rutledge, S. Jonzzon, E.A. Winkler, D. Raper, M.T. Lawton, A.A. Abla, Small Aneurysms with Low PHASES Scores Account for Most Subarachnoid Hemorrhage Cases, World Neurosurg. 139 (2020) e580–e584. https://doi.org/10.1016/j.wneu.2020.04.074.

[8]     P.R. Hoskins, P. V. Lawford, B.J. Doyle, Cardiovascular Biomechanics, 2017. https://doi.org/10.1007/978-3-319-46407-7.

[9]     J. Alastruey, K.H. Parker, S.J. Sherwin, Arterial pulse wave haemodynamics, in: BHR Gr. - 11th Int. Conf. Press. Surges, 2012: pp. 401–442.

[10]    C. R. Ethier and C. A. Simmons, Introductory Biomechanics From Cells to Organisms, 2007.

[11]    W.W. Nichols, M.F. O'Rourke, C. Vlachopoulos, A.P. Hoeks, R.S. Reneman, McDonald's blood flow in arteries theoretical, experimental and clinical principles, Sixth Edit, Hodder and Stoughton Ltd, a division of Hachette UK, London, 2011. https://doi.org/10.1111/j.1540-8175.1991.tb01207.x.

[12]    M.S. Olufsen, C.S. Peskin, W.Y. Kim, E.M. Pedersen, A. Nadim, J. Larsen, Numerical simulation and experimental validation of blood flow in arteries with structured-tree outflow conditions, Ann. Biomed. Eng. 28 (2000) 1281–1299. https://doi.org/10.1114/1.1326031.

[13]    N. Stergiopulos, P. Segers, N. Westerhof, Use of pulse pressure method for estimating total arterial compliance in vivo, Am. J. Physiol. - Hear. Circ. Physiol. 276 (1999). https://doi.org/10.1152/ajpheart.1999.276.2.h424.

[14]    R.D. Latham, N. Westerhof, P. Sipkema, B.J. Rubal, P. Reuderink, J.P. Murgo, Regional wave travel and reflections along the human aorta: A study with six simultaneous micromanometric pressures, Circulation. 72 (1985) 1257–1269. https://doi.org/10.1161/01.CIR.72.6.1257.

[15]    J.D. Humphrey, C.A. Taylor, Intracranial and abdominal aortic aneurysms: Similarities, differences, and need for a new class of computational models, Annu. Rev. Biomed. Eng. 10 (2008) 221–246. https://doi.org/10.1146/annurev.bioeng.10.061807.160439.

[16]    P.A. Cahill, E.M. Redmond, Vascular endothelium - Gatekeeper of vessel health, Atherosclerosis. 248 (2016) 97–109. https://doi.org/10.1016/j.atherosclerosis.2016.03.007.

[17]    A.M. Malek, S.L. Alper, Heamodynamics Shear stress and Its Role in Atherosclerosis, Stress Int. J. Biol. Stress. 282 (1999) 2035–2042.

[18]    J.M. Dolan, J. Kolega, H. Meng, High wall shear stress and spatial gradients in vascular pathology: A review, Ann. Biomed. Eng. (2013). https://doi.org/10.1007/s10439-012-0695-0.

[19]    J.J. Chiu, S. Chien, Effects of disturbed flow on vascular endothelium: Pathophysiological basis and clinical perspectives, Physiol. Rev. 91 (2011) 327–387. https://doi.org/10.1152/physrev.00047.2009.

[20]    A.E. Murphy SL, Xu JQ, Kochanek KD, Mortality in the United States, 2017 Key findings Data from the National Vital Statistics System, NCHS Data Brief. (2018) 1–8.

[21]  K.D. Kochanek, S.L. Murphy, J. Xu, E. Arias, Deaths: Final data for 2014, Natl. Vital Stat. Reports. 68 (2016) 1–18.

[22]  M. Nichols, N. Townsend, M. Rayner, European cardiovascular disease statistics, 2012.

[23]  H. Meng, V.M. Tutino, J. Xiang, A. Siddiqui, High WSS or Low WSS? Complex interactions of hemodynamics with intracranial aneurysm initiation, growth, and rupture: Toward a unifying hypothesis, Am. J. Neuroradiol. 35 (2014) 1254–1262. https://doi.org/10.3174/ajnr.A3558.

[24]  N. Ajiboye, N. Chalouhi, R.M. Starke, M. Zanaty, R. Bell, Unruptured Cerebral Aneurysms: Evaluation and Management, Sci. World J. 2015 (2015). https://doi.org/10.1155/2015/954954.

[25]  O. Tanweer, T.A. Wilson, E. Metaxa, H.A. Riina, H. Meng, A Comparative Review of the Hemodynamics and Pathogenesis of Cerebral and Abdominal Aortic Aneurysms: Lessons to Learn From Each Other, J. Cerebrovasc. Endovasc. Neurosurg. 16 (2014) 335. https://doi.org/10.7461/jcen.2014.16.4.335.

[26]  B. Williams, G. Mancia, W. Spiering, E.A. et al. Rosei, 2018 ESC/ESH Guidelines for the management of arterial hypertension, Eur. Heart J. 39 (2018) 3021–3104. https://doi.org/10.1093/eurheartj/ehy339.

[27]  H. Scott, M.J. Barton, A.N.B. Johnston, Isolated systolic hypertension in young males: a scoping review, Clin. Hypertens. 27 (2021) 1–12. https://doi.org/10.1186/s40885-021-00169-z.

[28]  N. Westerhof, J.W. Lankhaar, B.E. Westerhof, The arterial windkessel, Med. Biol. Eng. Comput. 47 (2009) 131–141. https://doi.org/10.1007/s11517-008-0359-2.

[29]  A. Noordergraaf, P.D. Verdouw, H.B.K. Boom, The use of an analog computer in a circulation model, Prog. Cardiovasc. Dis. 5 (1963) 419–439. https://doi.org/10.1016/S0033-0620(63)80009-2.

[30]  N. Westerhof, F. Bosman, C.J. De Vries, A. Noordergraaf, Analog studies of the human systemic arterial tree, J. Biomech. 2 (1969) 121–143. https://doi.org/10.1016/0021-9290(69)90024-4.

[31]  A. Jonášová, J. Vimmr, Noninvasive assessment of carotid artery stenoses by the principle of multiscale modelling of non-Newtonian blood flow in patient-specific models, Appl. Math. Comput. 319 (2018) 598–616. https://doi.org/10.1016/j.amc.2017.07.032.

[32]  R.L. Spilker, C.A. Taylor, Tuning multidomain hemodynamic simulations to match physiological measurements, Ann. Biomed. Eng. 38 (2010) 2635–2648. https://doi.org/10.1007/s10439-010-0011-9.

[33]  J.-F.G. and I.E.V.-C. S. Pant, B.Fabrèges, A methodological paradigm for patient-specific multi-scale CFD simulations: from clinical measurements to parameter estimates for individual analysis, Int. J. Numer. Meth. Biomed. Engng. 30 (2014) 1614–1648. https://doi.org/10.1002/cnm.

[34]  A. Jonášová, J. Vimmr, On the relevance of boundary conditions and viscosity models in blood flow simulations in patient-specific aorto-coronary bypass models, Int. j. Numer. Method. Biomed. Eng. (2021) 1–30. https://doi.org/10.1002/cnm.3439.

[35]  J. Jagos, J. Kohut, M. Kotek, P. Skacel, J. Bursa, Influence of Turbulence in Aorta-like Tube: Computational and Experimental Study, J. Appl. Fluid Mech. 14 (2021) 1411–1420. https://doi.org/10.47176/jafm.14.05.32291.

[36]  M.C. Brindise, P.P. Vlachos, Pulsatile pipe flow transition: Flow waveform effects, Phys. Fluids. 30 (2018). https://doi.org/10.1063/1.5021472.

[37]  E. Özahi, M.Ö. Çarpınlıoğlu, A non-dimensional oscillation parameter describing interactive influence of oscillation frequency and velocity amplitude ratio for use in pulsatile flows, Meas. J. Int. Meas. Confed. 99 (2017) 36–43. https://doi.org/10.1016/j.measurement.2016.12.018.

[38]  M. Xenos, Y. Alemu, D. Zamfir, S. Einav, J.J. Ricotta, N. Labropoulos, A. Tassiopoulos, D. Bluestein, The effect of angulation in abdominal aortic aneurysms: Fluid-structure interaction simulations of idealized geometries, Med. Biol. Eng. Comput. 48 (2010) 1175–1190. https://doi.org/10.1007/s11517-010-0714-y.

[39]     F. Gao, H. Ueda, L. Gang, H. Okada, Fluid structure interaction simulation in three-layered aortic aneurysm model under pulsatile flow: Comparison of wrapping and stenting, J. Biomech. 46 (2013) 1335–1342. https://doi.org/10.1016/j.jbiomech.2013.02.002.

[40]     C.J. Drewe, L.P. Parker, L.J. Kelsey, P.E. Norman, J.T. Powell, B.J. Doyle, Haemodynamics and stresses in abdominal aortic aneurysms: A fluid-structure interaction study into the effect of proximal neck and iliac bifurcation angle, J. Biomech. 60 (2017) 150–156. https://doi.org/10.1016/j.jbiomech.2017.06.029.

[41]     P. Reymond, Y. Bohraus, F. Perren, F. Lazeyras, N. Stergiopulos, Validation of a patient-specific one-dimensional model of the systemic arterial tree, Am. J. Physiol. - Hear. Circ. Physiol. 301 (2011) 1173–1182. https://doi.org/10.1152/ajpheart.00821.2010.

[42]     P. Reymond, P. Crosetto, S. Deparis, A. Quarteroni, N. Stergiopulos, Physiological simulation of blood flow in the aorta: Comparison of hemodynamic indices as predicted by 3-D FSI, 3-D rigid wall and 1-D models, Med. Eng. Phys. 35 (2013) 784–791. https://doi.org/10.1016/j.medengphy.2012.08.009.

[43]     D.H. Bergel, Viscoelastic properties of the arterial wall, Queen Mary University of London, 1960.

[44]     K.H. Parker, An introduction to wave intensity analysis, Med. Biol. Eng. Comput. 47 (2009) 175–188. https://doi.org/10.1007/s11517-009-0439-y.

[45]     R.G. Gosling, D.L. Newman, N.L. Bowden, K.W. Twinn, The area ratio of normal aortic junctions. Aortic configuration and pulse-wave reflection., Br. J. Radiol. 44 (1971) 850–853. https://doi.org/10.1259/0007-1285-44-527-850.

[46]     S.E. Greenwald, A.C. Carter, C.L. Berry, Effect of age on the in vitro reflection coefficient of the aortoiliac bifurcation in humans, Circulation. 82 (1990) 114–123. https://doi.org/10.1161/01.CIR.82.1.114.

[47]     L.P. Parker, J.T. Powell, L.J. Kelsey, B. Lim, R. Ashleigh, M. Venermo, I. Koncar, P.E. Norman, B.J. Doyle, Morphology and Hemodynamics in Isolated Common Iliac Artery Aneurysms Impacts Proximal Aortic Remodeling, Arterioscler. Thromb. Vasc. Biol. 39 (2019) 1125–1136. https://doi.org/10.1161/ATVBAHA.119.312687.

[48]     J.K.J. Li, Dominance of geometric over elastic factors in pulse transmission through arterial branching, Bull. Math. Biol. 48 (1986) 97–103. https://doi.org/10.1016/s0092-8240(86)90023-6.

[49]     F.H. Messerli, B. Williams, E. Ritz, Essential hypertension, Lancet. 370 (2007) 591–603. https://doi.org/10.1016/S0140-6736(07)61299-9.

[50]     J. Jagos, D. Schwarz, S. Polzer, J. Bursa, Effect of aortic bifurcation geometry on pressure and peak wall stress in abdominal aorta : Fluid-structure interaction study, Med. Eng. Phys. 118 (2023) 1–8. https://doi.org/10.1016/j.medengphy.2023.104014.

[51]     S. Roccabianca, C.A. Figueroa, G. Tellides, J.D. Humphrey, Quantification of regional differences in aortic stiffness in the aging human, J. Mech. Behav. Biomed. Mater. 29 (2014) 618–634. https://doi.org/10.1016/j.jmbbm.2013.01.026.

[52]     S.K. Aytac, H. Yigit, T. Sancak, H. Ozcan, Correlation between the diameter of the main renal artery and the presence of an accessory renal artery: Sonographic and angiographic evaluation, J. Ultrasound Med. 22 (2003) 433–439. https://doi.org/10.7863/jum.2003.22.5.433.

[53]     P.M. O'Flynn, G. O'Sullivan, A.S. Pandit, Geometric variability of the abdominal aorta and its major peripheral branches, Ann. Biomed. Eng. 38 (2010) 824–840. https://doi.org/10.1007/s10439-010-9925-5.

[54]     O.H. Yeoh, Some forms of the strain energy function for rubber, Rubber Chem. Technol. 66 (1993) 754–771. https://doi.org/10.5254/1.3538343.

[55]     L. Horny, T. Adamek, E. Gultova, R. Zitny, J. Vesely, H. Chlup, S. Konvickova, Correlations between age, prestrain, diameter and atherosclerosis in the male abdominal aorta, J. Mech.

Behav. Biomed. Mater. 4 (2011) 2128–2132. https://doi.org/10.1016/j.jmbbm.2011.07.011.

[56]   M.W. Siebert, P.S. Fodor, Newtonian and Non-Newtonian Blood Flow over a Backward- Facing Step – A Case Study, Excerpt from Proc. COMSOL Conf. 2009 Bost. (2009) 5.

[57]   S.E. Maier, M.B. Scheidegger, K. Liu, E. Schneider, A. Bellinger, P. Boesiger, Renal artery velocity mapping with MR imaging, J. Magn. Reson. Imaging. 5 (1995) 669–676. https://doi.org/10.1002/jmri.1880050609.

[58]   I.E. Vignon-Clementel, C. Alberto Figueroa, K.E. Jansen, C.A. Taylor, Outflow boundary conditions for three-dimensional finite element modeling of blood flow and pressure in arteries, Comput. Methods Appl. Mech. Eng. 195 (2006) 3776–3796. https://doi.org/10.1016/j.cma.2005.04.014.

[59]   H.C. Groen, L. Simons, Q.J.A. van den Bouwhuijsen, E.M.H. Bosboom, F.J.H. Gijsen, A.G. van der Giessen, F.N. van de Vosse, A. Hofman, A.F.W. van der Steen, J.C.M. Witteman, A. van der Lugt, J.J. Wentzel, MRI-based quantification of outflow boundary conditions for computational fluid dynamics of stenosed human carotid arteries, J. Biomech. 43 (2010) 2332–2338. https://doi.org/10.1016/j.jbiomech.2010.04.039.

[60]   C.M. McEniery, Yasmin, I.R. Hall, A. Qasem, I.B. Wilkinson, J.R. Cockcroft, Normal vascular aging: Differential effects on wave reflection and aortic pulse wave velocity - The Anglo-Cardiff Collaborative Trial (ACCT), J. Am. Coll. Cardiol. 46 (2005) 1753–1760. https://doi.org/10.1016/j.jacc.2005.07.037.

[61]   A.Vieli U.Moser S.Maier D.Meier P.Boesiger, Velocity profiles in the normal human abdominal aorta: A comparison between ultrasound and magnetic resonance data, Ultrasound Med. Biol. 15 (1989) 113–119.

[62]   J.F. Vollmar, P. Pauschinger, E. Paes, E. Henze, A. Friesch, Aortic Aneurysms As Late Sequelae of Above-Knee Amputation, Lancet. 334 (1989) 834–835. https://doi.org/10.1016/S0140-6736(89)92999-1.

[63]   Y. Hoi, B.A. Wasserman, Y.J. Xie, S.S. Najjar, L. Ferruci, E.G. Lakatta, G. Gerstenblith, D.A. Steinman, Characterization of volumetric flow rate waveforms at the carotid bifurcations of older adults, Physiol. Meas. 31 (2010) 291–302. https://doi.org/10.1088/0967-3334/31/3/002.

[64]   J. Hashimoto, B.E. Westerhof, S. Ito, Carotid Flow Augmentation, Arterial Aging, and Cerebral White Matter Hyperintensities: Comparison with Pressure Augmentation, Arterioscler. Thromb. Vasc. Biol. 38 (2018) 2843–2853. https://doi.org/10.1161/ATVBAHA.118.311873.

[65]   K. Hirata, T. Yaginuma, M.F. O'Rourke, M. Kawakami, Age-related changes in carotid artery flow and pressure pulses: Possible implications for cerebral microvascular disease, Stroke. 37 (2006) 2552–2556. https://doi.org/10.1161/01.STR.0000242289.20381.f4.

[66]   D.W. Holdsworth, C.J.D. Norley, R. Frayne, D.A. Steinman, B.K. Rutt, Characterization of common carotid artery blood-flow waveforms in normal human subjects, Physiol. Meas. 20 (1999) 219–240. https://doi.org/10.1088/0967-3334/20/3/301.

[67]   K.T. Ong, S. Delerme, B. Pannier, M.E. Safar, A. Benetos, S. Laurent, P. Boutouyrie, Aortic stiffness is reduced beyond blood pressure lowering by short-term and long-term antihypertensive treatment: A meta-analysis of individual data in 294 patients, J. Hypertens. 29 (2011) 1034–1042. https://doi.org/10.1016/S0140-6736(16)31134-5.

[68]   M.E. Safar, Arterial aging-hemodynamic changes and therapeutic options, Nat. Rev. Cardiol. 7 (2010) 442–449. https://doi.org/10.1038/nrcardio.2010.96.

[69]   M.J. Mulvany, Small artery remodelling in hypertension: Causes, consequences and therapeutic implications, Med. Biol. Eng. Comput. 46 (2008) 461–467. https://doi.org/10.1007/s11517-008-0305-3.

[70]   Y. Hoi, B.A. Wasserman, E.G. Lakatta, D.A. Steinman, Carotid bifurcation hemodynamics in older adults: Effect of measured versus assumed flow waveform, J. Biomech. Eng. 132 (2010) 1–6. https://doi.org/10.1115/1.4001265.

[71] M.D. Ford, N. Alperin, H.L. Sung, D.W. Holdsworth, D.A. Steinman, Characterization of volumetric flow rate waveforms in the normal internal carotid and vertebral arteries, Physiol. Meas. 26 (2005) 477–488. https://doi.org/10.1088/0967-3334/26/4/013.

[72] P. MARCIÁN, O. KONEČNÝ, L. BORÁK et al., On the Level of Computational Models in Biomechanics Depending on Gained Data from Ct/Mri and Micro- Ct, in: MENDEL 2011 - 17th Int. Conf. Soft Comput., Brno University of Technology, Brno, 2011: pp. 455–462.

[73] S.W. Lee, L. Antiga, J.D. Spence, D.A. Steinman, Geometry of the carotid bifurcation predicts its exposure to disturbed flow, Stroke. 39 (2008) 2341–2347. https://doi.org/10.1161/STROKEAHA.107.510644.

[74] L. Grinberg, G.E. Karniadakis, Outflow boundary conditions for arterial networks with multiple outlets, Ann. Biomed. Eng. 36 (2008) 1496–1514. https://doi.org/10.1007/s10439-008-9527-7.

[75] F. Rikhtegar, J.A. Knight, U. Olgac, S.C. Saur, D. Poulikakos, W. Marshall, P.C. Cattin, H. Alkadhi, V. Kurtcuoglu, Choosing the optimal wall shear parameter for the prediction of plaque location-A patient-specific computational study in human left coronary arteries, Atherosclerosis. 221 (2012) 432–437. https://doi.org/10.1016/j.atherosclerosis.2012.01.018.

[76] C. Irace, C. Carallo, M.S. De Franceschi, F. Scicchitano, M. Milano, C. Tripolino, F. Scavelli, A. Gnasso, Human common carotid wall shear stress as a function of age and gender: A 12-year follow-up study, Age (Omaha). 34 (2012) 1553–1562. https://doi.org/10.1007/s11357-011-9318-1.

[77] X. Zhao, M. Zhao, S. Amin-Hanjani, X. Du, S. Ruland, F.T. Charbel, Wall Shear Stress in Major Cerebral Arteries as a Function of Age and Gender-A Study of 301 Healthy Volunteers, J. Neuroimaging. 25 (2015) 403–407. https://doi.org/10.1111/jon.12133.

[78] G.R. Drummond, A. Vinh, T.J. Guzik, C.G. Sobey, Immune mechanisms of hypertension, Nat. Rev. Immunol. 19 (2019) 517–532. https://doi.org/10.1038/s41577-019-0160-5.

[79] G. Gallo, M. Volpe, C. Savoia, Endothelial Dysfunction in Hypertension: Current Concepts and Clinical Implications, Front. Med. 8 (2022) 1–8. https://doi.org/10.3389/fmed.2021.798958.

[80] J. Malik, L. Novakova, A. Valerianova, E. Chytilova, V. Lejsek, K. Buryskova Salajova, L. Lambert, T. Grus, M. Porizka, P. Michalek, Wall Shear Stress Alteration: a Local Risk Factor of Atherosclerosis, Curr. Atheroscler. Rep. 24 (2022) 143–151. https://doi.org/10.1007/s11883-022-00993-0.

[81] A. Virdis, L. Ghiadoni, S. Taddei, Effects of antihypertensive treatment on endothelial function, Curr. Hypertens. Rep. 13 (2011) 267–281. https://doi.org/10.1007/s11906-011-0207-x.

# Curriculum vitae

**Personal details**

| | |
|---|---|
| Name | Jiří Jagoš |
| Date of birth | 29.4. 1992 |
| Address | Velká nad Veličkou 427, 696 74 Velká nad Veličkou |
| E-mail | Jiri.Jagos@vutbr.cz |

**Education**

| | |
|---|---|
| 2018 − present | Applied Mechanics (doctoral study) |
| | Brno University of Technology |
| | Faculty of Mechanical Engineering |
| 2014 − 2016 | Engineering Mechanics and Biomechanics (Master's degree) |
| | Brno University of Technology |
| | Faculty of Mechanical Engineering |
| 2011 − 2014 | Mechanical Engineering (Bachelor's degree) |
| | Brno University of Technology |
| | Faculty of Mechanical Engineering |

**Career overview**

| | |
|---|---|
| 8/2022 − present | Assistant professor (Part-time) |
| | Institute of Solid Mechanics, Mechatronics and Biomechanics |
| | Faculty of Mechanical Engineering |
| | Brno University of Technology |
| 1/2021 – 5/2022 | R&D Engineer (Part-time) |
| | CKD Blansko Holding, a.s. |
| | Blansko, Czech Republic |
| 8/2016 – 10/2018 | CFD/FEM analysis Engineer (Full-time) |
| | Evektor, spol. s.r.o. |
| | Mladá Boleslav, Czech Republic |

**Languages**

English (level C1)

**Computer skills**

Ansys APDL, Fluent, ANSA, FEMUP, Matlab/Simulink, SOLIDWORKS